Shear-banding predictions for wormlike micellar systems under a contraction-expansion complex flow

J. Esteban López-Aguilar[a,b,*], Hamid R. Tamaddon-Jahromi[b], Octavio Manero[c]

[a]Facultad de Química, Departamento de Ingeniería Química, Universidad Nacional Autónoma de México (UNAM), Ciudad Universitaria, Coyoacán, CDMX, 04510, Mexico; [b]Institute of Non-Newtonian Fluid Mechanics, Swansea University, Faculty of Science and Engineering, Bay Campus, Fabian Way, Swansea, SA1 8EN, West Glamorgan, United Kingdom; [c]Instituto de Investigaciones en Materiales, Universidad Nacional Autónoma de México, 04510, Mexico.

Abstract

This study focuses on computational modelling of *shear-banded* wormlike micellar solutions in a complex planar Couette-flow, driven by a moving top-plate over a rounded-corner 4:1:4 obstruction. The BMP+_τ_p constitutive model is used, which is constructed within an Oldroyd-B-like form, coupled with a thixotropic fluidity-based internal-structure equation. Here, solute energy-dissipation drives fluid-structure adjustment in a construction-destruction dynamics affected by viscoelasticity. This model reproduces conventional wormlike micellar solution key features, such as shear-thinning, extensional hardening/softening, viscoelasticity, apparent yield-stress and shear-banding, with a bounded extensional-viscosity and an N_{1Shear}-upturn at high deformation-rates. The BMP+_τ_p characterisation for shear-banding solutions is based on extremely low solvent-fractions $\beta \leq 10^{-2}$ and appropriate shear-banding intensity-parameters. Ensuing flow-structure is analysed through velocity, stress and fluidity fields, whereupon banded and non-banded system response is contrasted at appropriately selected flow-rates. Highly non-linear solutions are obtained with our hybrid *fe-fv* algorithm, capturing essential shear-banded flow features reported experimentally. For a fluid exhibiting banding behaviour, banded-solutions are generated at an intermediate flow-rate within the flow-curve unstable branch. Here, in the fully-developed simple-shear flow away from the contraction, a split velocity-profile is observed, with different viscosity bands at equal stress-levels, enhanced with a shock-capture procedure. Non-banded solutions are derived for the lowest and highest flow-rates sampled, which are located in the stable branches. Within the constriction zone, the banded profiles are lost due to the mixed non-homogeneous shear-to-extensional deformation. Comparatively, shear-banding fluids display less intense viscosity and stress features, which are correlated with their relatively stronger shear-thinning response. The constriction resistance results in a pressure-level adjustment, leading to fully-developed Couette-like constant values upstream-downstream.

Keywords: shear-banding, complex-flow, wormlike micelles, revisited Bautista-Manero models, numerical simulation, hybrid finite element/volume method, enhanced oil-recovery

* Author for correspondence, email: jelopezaguilar@unam.mx

I. Introduction

The theme of this predictive finite volume/element modelling study is particularly concerned with investigating material system response of worm-like micellar solutions. These solutions are capable of supporting shear-banding under ideal shear-flow. To further develop and identify the corresponding position adopted in inhomogeneous complex flow, a modified planar Couette-flow is considered. This flow is generated by a moving top-plate in a rounded-corner 4:1:4 planar contraction-expansion geometry (aspect-ratio α=4), see Fig.1. To avoid singular flow response, the obstruction formed has a rounded-tip . This leads to the observation of pure-shear Couette-flow in fully-developed entry-exit regions, away from the obstruction, whilst mixed shear-extensional flow arises around the contraction-zone. This provides the possibility to gather zones of pure shear-banding in the entry flow-region, allowing to study the corresponding system response within and beyond the complex flow zone, once exit-flow pure-shear conditions are recovered.[†]

Shear-banded flows have been traditionally studied within the restricted context of ideal shear-flow.[1-6] In the planar Couette flow under present consideration, shear-banded flow is observed in the form of a discontinuous velocity-gradient profile. This profile displays two or more distinct shear-rates over multiple bands, which are constant over each band, while simultaneously maintaining equitable total shear-stress levels across each band.[5] This scenario is reflected in an idealised simple-shear flow-curve, which covers a range of shear-rates in the stable branches of the flow-curve, each shear-rate with its equivalent distinct shear-stress level. The level of shear-stress itself is determined by the characteristic shear-rate U_{plate}/L (which is directly linked to the generated flow-rate). Here, U_{plate} represents a moving-wall top-plate velocity, and L is the width of the flow-cell. One notes that to generate a banded-flow, the overall characteristic shear-rate (U_{plate}/L) must lie within the unstable shear-rate range regime of the flow curve, which is identified in a negative stress-slope, plotted against shear-rate rise.[3,5-7]

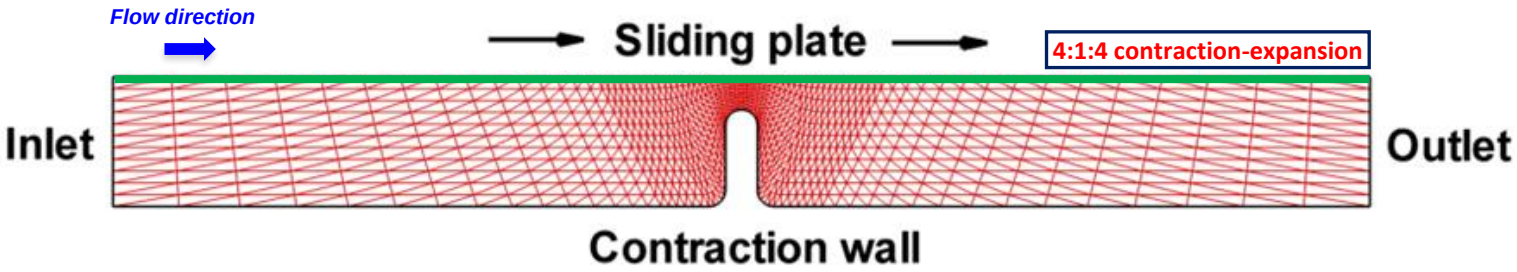

Figure 1. Schematics of the planar *modified* Couette geometry – This complex flow geometry is a composition of a 4:1:4 planar contraction-expansion with rounded edges and a drag flow. The flow is promoted by the drag the sliding plate exerts on the fluid stick to its surface. One observes simple-shear flow away from the contraction and mixed shear-to-extensional flow in the contraction neighbourhood.

[†] To suit present purposes, the simplicity of plane Couette flow is preferred (with its single-rate non-SB). The multiple form of rate-profiles, as offered by a pressure-driven deformation, and banding in extensional deformations under extension-necking conditions, are seen as a more advanced stages in problem resolution, which will appear subsequently.

Materials that exhibit the phenomenon of shear-banding are wide-ranging. For example, shear-banded inhomogeneous flow may be observed in aqueous surfactant solutions, pastes, foams, emulsions, granular slurries, liquid crystals, concentrated colloidal emulsions and suspensions, and oil-fractions.[3-6] Despite the large variety of materials capable of displaying bands in complex-flow under realistic scenarios and their widespread industrial use, the majority of previous work has been limited to idealised steady simple-shear flow. Commonly, this scenario has been analysed through simple-shear Couette-flow and Taylor-Couette-type deformations (promoted by surface movement and corresponding drag flow in steady and oscillatory shear protocols).[3-8] In addition, extension-necking has been observed in some wormlike micelle systems,[9,10] in the form of extensional deformation-rate localisation, that originates from a multiple-valued extensional-stress flow-curve, with higher extension-rates and pronounced thinning of the filament radius in the middle-plane of the sample. Despite such advance, there has been a distinct lack of attention paid to the response of banding-fluids in complex flow with tangible sparsity in the literature on either experimental or predictive studies.[11-15] Hence the present study focuses on inhomogeneous modified Couette-flow (with spatial dimension greater than one), and the derivation of numerical solutions for wormlike micellar banding-fluids.

Olmsted[3] states two general modes of shear-banding for shear-thinning and shear-thickening fluids: *(i) gradient-banding*, in which bands of different apparent viscosities coexist, under a common overall shear-stress, and; *(ii) vorticity-banding*, in which bands with different shear-stress distribute in the vorticity direction. Divoux et al.[6] review two main types of soft-matter that undergo segregation due to shear-banding: *(i) fluid-like materials*, in which semi-dilute polymeric- and wormlike micellar solutions are grouped; and *(ii) soft-glassy materials*, which correspond to more concentrated materials than common wormlike micellar solutions, may display liquid or gel-like features (principally yield-stress) at rest. These complex fluids exhibit shear-banding through a gradient-banding mechanism, which is captured via a non-monotonic flow curve. Such behaviour is observed in the experiments of Fischer & Rehage[16] and Pipe et al.,[17] where shear-stress plateaux are apparent over finite shear-rate ranges. In complex flow, particularly in microfluidic planar contractions, Nodoushan et al.[15] recently reported intense secondary flow promoted by the interplay of strong shear-thinning, shear-banding and yield-stress for typical cetyltrimethylammonium bromide/sodium salicylate wormlike micellar solutions.

One of the key features for a model to predict banded flow is its capacity to support a non-monotonic flow-curve with localised extrema.[3,5-7] Two main streams of constitutive modelling have been developed to predict shear-banding: a classical approach in polymeric fluids;[18-20] and alternatively equations of state based on the description of the fluid microstructure.[17,21-24]

On the side of polymer-based constitutive models, a modified Johnson–Segalman model characterises banding-materials via a diffusion term in the polymeric extra-stress equation, leading to the so-called d-JS model of Olmsted *et al.*.[18] Such stress-diffusion term in the polymeric stress equation has the form of the Laplacian operator of the extra-stress tensor multiplied by a stress-diffusivity $\mathcal{D}$, i.e. $\mathcal{D}\nabla^2\boldsymbol{\tau}_p$. This particular model choice has captured

shear-bands in cylindrical Couette flow. In addition, wormlike micelles systems have also been represented through a form of Giesekus model, where shear-banding characteristics are introduced via the non-linear anisotropy coupling parameter.[20] These authors developed a method based on large amplitude oscillatory shear (LAOS) flow, from which fluid characterisation could be extracted, and where the onset of shear-banding was observed to depend on oscillation frequency.

Within the microstructural constitutive models, an extra structure equation(s) is used to induce non-monotonicity. The Vazquez-Cook-McKinley (VCM) model is one such, that is based on a discrete form of *'living polymer theory'*, attributed to Cates.[21] This *VCM-model* has been validated in simple flows where rheological homogeneity prevails, and under conditions of shear-banding.[17] A closely-related model to the VCM-model is the Germann-Cook-Beris (GCB) model, under which the structure breakage-rate depends explicitly on the trace of the conformation-tensor (always positive by definition).[8,22-23] Moreover, a soft glassy rheology (SGR) model has been recently proposed to model shear-banding under LAOS.[24] Similarly, solutions for startup in shear with the integral Doi-Edwards model,[25] have been compared to those obtained by Moorcroft and Fielding,[26] with a differential-approximation of the Rolie-Poly model. The Reactive-Rod Model (RRM) of Graham and co-workers[27,28] models wormlike micellar solutions as a suspension of rods that interact to form reversible physical bonds that modify the internal structure of the material. This RRM model predicts features of vorticity banding observed in diluted solutions.

In addition, the thixotropic Bautista-Manero-Puig (BMP) models also produce non-monotonic flow-curves through their dynamic fluid internal-structure equation. Such an additional fluid-structure evolution equation naturally integrates mechanisms for the construction and destruction of internal-structure.[29,30] This would include a structure destruction coefficient that has an explicit dependence on flow-invariants,[7,12,31] without the complication of handling Laplacian operators. For an approach to modelling shear-banding wormlike micellar solutions, the latest variant of which is the BMP+_τ_p, has been used previously under complex flow deformations, such as in circular contraction-expansion[29] and flow past a sphere[30]. The BMP+_τ_p has a destruction-parameter of linear-dependence on the second-invariant of rate-of-strain tensor. This model has the functional capability of generating a non-monotonic curve,[31]and importantly, a unique solution in the Shear-Banding (SB)-regime. This recent BMP+_τ_p model, and some previous variants, have incorporated a relationship between fluid-structure and viscoelasticity within the structure equation.[29-30] These developments have resulted in consistent energy-related pressure-drop predictions, whereas earlier versions were found to be inadequate.[32] In addition to supporting banded-flow, the latest BMP+_τ_p model also has a number of attractive rheological features, which include in shear, a second high-rate upturn in first-normal stress-difference N_{1Shear}; a bounded extensional-viscosity response; alongside extreme shear-thinning and strain-softening/hardening behaviour. These are all properties common to many wormlike micellar systems,[29-30] which are in agreement with experimental shear-flow findings.[16-17]

On the side of complex flow modelling, Varchanis et al.[14] conducted a comparison of the

predictive capabilities of well-known models under banding conditions in cross-slot and flow past a cylinder . These authors tested a model-proposal based on a fluidity variable against the Johnson-Segalman, the VCM and the Giesekus models. In addition, López-Aguilar et al.[12] and Hooshyar and Germann[13] carried out predictive work on the flow of wormlike micellar solutions in contraction geometries under banding conditions. Sasmal[33] performed computational modelling of non-banding wormlike micelles in expansion-contraction geometries using the VCM model. In pressure-driven tube flow, Cunha et al.[34] predicted transient shear-banding flow features with a fluidity-based constitutive model.

In this work, a BMP+_τ_p model[29-30] is used to represent the behaviour of wormlike micellar systems under shear-banding conditions, with an ingredient of complex flow posed by the constriction in the modified Couette geometry. This requires an additional term in the constitutive model with viscoelasticity within network-structure destruction kinetics, which can potentially facilitate shear-banding. Experimental evidence would indicate that extremely-concentrated micellar fluids with non-monotonic shear-stress, are required to generate shear-banded solutions. Therefore, banded-system response is sought under low solvent-fractions of $\beta \leq 10^{-2}$ and material shear-banding intensity parameters of $\zeta > 0$ ($\zeta = 0$, non-banding system), where non-monotonicity is observed in both shear stress and N_{1Shear}.

This article is organised as follows. First, section II provides details on the BMP+_τ_p model theoretical framework , along with its consequences on the relevant material-functions. This is accompanied by a range of suitable deformation-rates (converted into their corresponding flow-rates Q), that are used to characterise specific instances of low, intermediate and high deformation-rates. One must choose an intermediate deformation-rate such that the associated shear-stress lies on an unstable branch of the flow-curve, whilst corresponding low and high deformation-rates (with equal shear-stress) are located in stable branches. The combination of shear-rate and banding/non-banding fluids generates the various flow instances, which are analysed in Section III (Numerical Predictions). There, the banded complex-flow defines the main findings, while the remaining cases provide a backdrop for direct comparison. Finally in Section IV, the significant findings of the study are summarised.

II. Governing equations, constitutive modelling & theoretical framework

A. Conservation principles and BMP+_τ_p model

Wormlike micellar solutions are a type of complex fluids prone to generate banded-flows under specific conditions. According to experiments and conventional simple-shear flow modelling,[3,5-7], a combination of factors is necessary to particularly promote exposure to shear-banding: firstly, a *deformation-rate dependency* on the *destruction coefficient*; and secondly, *highly-concentrated micellar solutions*, with solvent-fractions on the order of $\beta \leq 10^{-2}$. In this work, the BMP+_τ_p model has been used to characterise the flow of wormlike micellar systems in complex flow.[29-30] With the BMP-family of fluids, non-monotonicity in the flow-curve is promoted through an explicit rate-dependent function, that acts on the structure-destruction coefficient k of the structure-equation, as expressed in Eq.(1).[31] This

function adopts a linear form of the second-invariant of the rate-of-deformation tensor $II_{\boldsymbol{D}}$, producted by a constant shear-banding intensity parameter (ϑ), viz. $k = k_0\left(1+\vartheta II_{\boldsymbol{D}}\right)$:

$$\left(\frac{\partial}{\partial t}+\boldsymbol{u}\cdot\nabla\right)f=\frac{1}{\lambda_s}\left(1-f\right)+k_0\left(1+\vartheta II_{\boldsymbol{D}}\right)\left(\frac{G_0\lambda_1}{\eta_\infty+\delta}-f\right)\left|\boldsymbol{\tau}_p:\boldsymbol{D}\right|. \qquad (1)$$

The structure-equation (Eq.(1)) provides an evolution equation for a dimensionless fluidity $f=\eta_{p0}/\eta_p$ (taken as scaled against a reference-viscosity, zero-rate solute-viscosity η_{p0}, with units of Pa·s). This equation establishes a coupled highly-nonlinear relationship between the structure dynamics, viscoelasticity and energy-dissipation. Within the *structure-destruction* term, the shear-banding intensity parameter ϑ appears in the destruction coefficient $k = k_0\left(1+\vartheta II_{\boldsymbol{D}}\right)$, and modulates the capacity of the fluid to generate banded flows. The ϑ-parameter appears in Eq.(1) in the form of a characteristic-time related to the appearance of flow-segregation. As a result, a new temporal-scale arises, which is closely linked to flow-segregation. At sufficiently high solute-concentrations, the shear-banding intensity parameter ϑ dictates the appearance of localised extrema (maxima-minima) in the flow-curve. Here the intensity of the shear-stress T_{xy} drops, marking a non-monotonic trend in the flow-curve, and then subsequently rises with deformation-rate increase. With ϑ=0, a monotonic T_{xy}-flow-curve is recovered. The structure-destruction term contribution to the structure-dynamics, is modulated through a base constant coefficient k_0, with units of inverse of stress (Pa^{-1}). The inverse of constant coefficient k_0 (i.e. k_0^{-1}), is related to a characteristic stress-level for structure-destruction. Note, the explicit presence of the relaxation-time λ_1 in Eq.(1) quantifies the viscoelastic contribution in the fluid-structure dynamics. There, G_0 represents the elastic modulus at vanishing deformation-rates and $(\eta_\infty+\delta)$ is the solute viscosity at high-deformation rates. Counterpart *structure-construction* dynamics is regulated via a structure-construction characteristic-time λ_s.

The fluidity *f* supplies the all-important information on the internal structure of the fluid at hand. It also acts to weight the polymeric-stress $\boldsymbol{\tau}_p$-contribution in a generalised Oldroyd-B-type differential statement, as follows:

$$\lambda_1\overset{\nabla}{\boldsymbol{\tau}}_p=2\eta_{p0}\boldsymbol{D}-f\boldsymbol{\tau}_p. \qquad (2)$$

In Eq.(2), the relaxation time λ_1 also modulates a second source of non-linearity; that is related to the upper-convected derivative of solute-stress, $\overset{\nabla}{\boldsymbol{\tau}}_p=\frac{\partial\boldsymbol{\tau}_p}{\partial t}+\boldsymbol{u}\cdot\nabla\boldsymbol{\tau}_p-\nabla\boldsymbol{u}^T\cdot\boldsymbol{\tau}_p-\boldsymbol{\tau}_p\cdot\nabla\boldsymbol{u}$.

This complex and highly-coupled rheological equation-of-state pairing (Eq.(1)-(2)), delivers the internal forces within the solute-component of such wormlike micellar fluids. It integrates with a complementary solvent Newtonian-contribution $\boldsymbol{\tau}_s = 2\eta_s \boldsymbol{D}$, to generate the total extra-stress $\boldsymbol{T} = \boldsymbol{\tau}_s + \boldsymbol{\tau}_p$; where η_s is the solvent viscosity. With this information, one seeks to preserve the mass and momentum conservation principles for incompressible and isothermal flow, expressed through the continuity equation and the momentum equation, respectively:

$$\nabla \cdot \boldsymbol{u} = 0\,, \tag{3}$$

$$\rho \frac{\partial \boldsymbol{u}}{\partial t} = \nabla \cdot \boldsymbol{T} - \rho \boldsymbol{u} \cdot \nabla \boldsymbol{u} - \nabla p\,. \tag{4}$$

Dimensionless forms for Eq.(1)-(4) and relevant dimensionless group numbers may be obtained by using the following dimensionless variables:

$$\boldsymbol{x}^* = \frac{\boldsymbol{x}}{L}\,,\quad \boldsymbol{u}^* = \frac{\boldsymbol{u}}{U}\,,\quad t^* = \frac{U}{L}t\,,\quad \boldsymbol{D}^* = \frac{L}{U}\boldsymbol{D}\,,\quad p^* = \frac{p}{\left(\eta_{p0}+\eta_s\right)\frac{U}{L}}\,,\ \boldsymbol{\tau}_p{}^* = \frac{\boldsymbol{\tau}_p}{\left(\eta_{p0}+\eta_s\right)\frac{U}{L}}\,.$$

Here, U represents a characteristic mean-velocity in the contraction gap, originating from the flow-rate per unit width Q. L is the width of the flow-cell, from which a characteristic deformation-rate (U/L) may be defined. Hence, time is non-dimensionalised using the characteristic deformation-rate (U/L). Forces, expressed in terms of pressure and stresses, are normalised with respect to the characteristic stress as measured in the first Newtonian-plateau, i.e. $\left[\left(\eta_{p0}+\eta_s\right)(U/L)\right]$. Thus, non-dimensionalisation of Eq.(1)-(4), yields the following dimensionless group numbers: in Eq.(1) and in the form of characteristic-times, (i) a dimensionless shear-banding intensity parameter, $\zeta = \vartheta(U/L)$, (ii) a dimensionless structure-construction characteristic-time, $\omega = \lambda_s (U/L)$, and (iii) the Weissenberg group-number, $Wi = \lambda_1 (U/L) = \lambda_1 Q / L^2$, which can be interpreted as an additional viscoelastic dimensionless time-scale.‡ Alternatively, in Eq.(1), in the form of normalised stresses, (iv) two dimensionless structure-destruction parameters arise, i.e. $\xi_{G_0} = \left[k_0 G_0 / \left(\eta_\infty + \delta\right)\right]\left(\eta_{p0}+\eta_s\right)$ and $\xi = k_0\left(\eta_{p0}+\eta_s\right)(U/L)$. One of them, ξ_{G_0}, compares the elastic modulus of the material against its structure-destruction stress, producted with a viscosity ratio. In contrast, ξ normalises the characteristic total stress at the first Newtonian-plateau with respect to the structure-destruction characteristic stress. In addition, from Eq.(2) and $\boldsymbol{T}$-definition, a solvent-fraction $\beta = \eta_s / \left(\eta_{p0}+\eta_s\right)$ may be defined. The solvent-fraction

‡ Here, λ_1 is taken as 1 s.

β expresses a relative measure of the solvent-viscosity to the total viscosity at zero deformation-rate, i.e. $\eta_{p0}+\eta_s$. β may be used to estimate the relative solvent-to-solute composition in the viscoelastic wormlike micellar solution. The corresponding (variable) viscosity of the wormlike micellar solution is $\eta_{Tot}=\eta_p+\eta_s$. Finally, from Eq.(4), a non-dimensional group Reynolds number, $Re=\rho UL/\left(\eta_{p0}+\eta_s\right)$, also arises, based on a material density ρ. The *Re*-number regulates the relative contribution of inertial forces with respect to diffusive forces acting on the material. Inertial forces effects are taken as negligible in the present work, i.e. *Re*~O(10^{-2}), with its companion implication of inertialess creeping flow.

B. Material functions, flow-domain and alternative deformation-rate choices

Fig.2a provides the steady-state flow-curves for total shear-stress T_{xy} against shear-rate covering two representative fluids: i) a non-shear-banding fluid (characterised by a null shear-banding intensity-parameter ζ=0); and ii) a banding fluid (with ζ=3), see first column of Table 1. The common feature across this data is the need for an extremely low solvent-fraction, specifically β=10^{-2}, to generate non-monotonic flow-curves in the case where $\zeta\neq0$.[3,5-7] The characteristic cubic non-monotonic T_{xy}-shape in Fig.2a is manifested by the presence of local maxima (rate 10^0) and minima (rate 10^1), which allow for the same constant state level of stress to be sustained by two different shear-rate.

Further rheology of interest lies in the shear-thinning and extension-hardening profiles shown in Fig.2b, which are promoted by the set of structure construction-destruction kinetic-parameters employed {ω, ξ_{G0}, ξ}={4, 0.1136, 2.27x10^{-7}} (see Table 2, for the full set of parameters used in this work). The extent of thinning covers a rapid drop over two-decade, supported by solvent-fraction (β=10^{-2}). As illustrated in Fig.2b, the slope-of-decline is influenced by elevation in shear-banding parameter, where a rise in ζ promotes shear-thinning. This is reflected in the power-law index equivalents of *n*=0.196 for (ζ=0), and *n*=-0.142 for (ζ=3). The negative value of *n* is associated with stress non-monotonicity.[35]

Furthermore, some moderate extensional-hardening is detected in Fig.2b around unity rates in both shear-banding and non-shear-banding fluids equally, proving to be indistinguishable in this deformation[§]. The position in shear viscosity is reflected through the corresponding response in N_{1Shear} profiles shown in Fig.2c, where the banding fluid displays a characteristic non-monotonic trend in N_{1Shear}, with clear and distinct local maxima (rate 10^0) and minima (rate ~10^4). Notably, the present BMP+_τ_p model predicts the N_{1Shear} upturn at high shear-rates (observed experimentally in wormlike micellar fluids; see Fig.2c);[16-17] and also, bounded extensional viscosity η_{Ext}-response at large extension-rates (Fig.2b).

[§] In this analysis, flow and material segregation is promoted primarily through shear-deformation. A second alternative for generating banded predictions is currently under development, which involves inhomogeneous shear and extensional deformations, namely, under extension-necking conditions.[9,10] Corresponding findings shall be published elsewhere.

Table 1. Deformation-rate versus fluid chart

	$\lambda_1\dot{\gamma}_0$ **=0.5** ***Q*=4**	$\lambda_1\dot{\gamma}_0$ **=3.75** ***Q*=30**	$\lambda_1\dot{\gamma}_0$ **=56** ***Q*=450**
ζ**=0** **non-shear-banding fluid**	Case A Non-banded	Case B Non-banded	Case C Non-banded
ζ**=3** **shear-banding fluid**	Case D Non-banded	**Case E** ***Banded***	Case F Non-banded

Table 2. List of parameters

Parameter (units)	Non shear-banding fluid	Shear-banding fluid
ζ (–)	0	3
β (–)	0.01	0.01
Ω (–)	4	4
ξ_{G0} (–)	0.1136	0.1136
ξ (–)	$2.27\text{x}10^{-7}$	$2.27\text{x}10^{-7}$
λ_1 (s)	1	1
Re (-)	10^{-2}	10^{-2}

An inflected, non-monotonic the flow-curve (Fig.2a), with predictions for homogeneous simple shear flow, is crucial in generating banded-solution. By examining these non-monotonic flow-curves, one can identify an unstable branch, which is characterised by a negative-sloped declining shear-stress zone (Fig.2a).[3,5-7] An unstable branch then stabilizes itself by generating shear-bands at the same stress level, but at alternative lower and/or higher shear-rates (stable-branches, with positive slopes). Each shear-band corresponds to a different degree of structure, which can macroscopically observed as viscosity or fluidity.

N_{1Shear}-banding- In Fig.3, the rheology is presented for a shear-banding fluid at three different solvent fraction levels. One notes that a plateau in T_{xy} is extracted, with a gradual elevation in solvent fraction, starting from the banding level of 10^{-2} up to 0.05. For $1.0>\beta\geq0.05$, the N_{1Shear}-data displays band-like features while providing an apparently monotonic trend in shear-stress (T_{xy}). The relevant mathematics for this scenario is expounded through the governing solute-content function. This is expressed through the *f*-functional of Eq.(5) in simple shear flow, where a cubic dependency on shear-rate is displayed, affecting stress thereby:

$$f^2-\left[1-\omega\xi\left(1+\zeta\dot{\gamma}\right)\left(1-\beta\right)\dot{\gamma}^2\right]f-\omega\xi\left(1+\zeta\dot{\gamma}\right)\xi_{G0}Wi\dot{\gamma}^2=0\,. \quad (5)$$

Recall also that the counterpart total shear-stress is $T_{xy}=\beta\dot{\gamma}+\left(1-\beta\right)\dot{\gamma}/f$ and the first normal-stress difference in shear is $N_{1Shear}=2Wi\left(1-\beta\right)\dot{\gamma}^2/f^2$. Unlike previous solutions, as shown and discussed in Fig.3b, (with banding promoted by non-monotonic-T_{xy}), in the *banded-regime* (***Case-E***), one might ask the question of what flow outcomes are possible under N_{1Shear}-banding alone. In Fig.3c, the fluidity appears relatively larger with β-rise.

In addition, in Fig.2, a comparison of the rheological response of our BMP+_τ_p is provided against the well-known Vazquez-Cook-McKinley (VCM) model.[21] This comparison is performed based on similar intensity in the peak of extensional viscosity η_{Ext}-response under β=10^{-2}. The parameter set of VCM displaying such behaviour is {C_{Aeq}, C_{Beq}, ξ, ε, μ}={0.5, 0.7, 0.42, 7.5x10^{-7}, 1.5}. As it is apparent in Fig.2b, the BMP+_τ_p and VCM η_{Ext}-trends appear similar for low to intermediate extension-rates up to the maximum η_{Ext}-level, located at $\lambda_1\dot{\varepsilon}$=0.5 units. Beyond this landmark, VCM displays a stronger strain-softening trend towards the second Newtonian-plateau. Interestingly and relevant to this work, BMP+_τ_p and VCM produce a non-monotonic shear-stress flow-curve, whose unstable branches are located in the shear-rate range of $1\leq\lambda_1\dot{\gamma}\leq30$ units (Fig.2a). Non-monotonicity is also observed in the first normal-stress in shear N_{1Shear}-measure for both models, but over the significantly extended shear-rate range of $1\leq\lambda_1\dot{\gamma}\leq10^4$ units (Fig.2c). Notably, in the unstable banding branches, VCM shear and normal stresses always lie at higher levels than those for BMP+_τ_p. As such, one would expect these two models to provide similar banding predictions in complex flow, as has already been reported recently by Varchanis et al..[14] A comparative study on predictive capabilities of these and other models in pressure-driven flow through constrictions and past objects will come subsequently, as well as analysis on extension necking situations in stretched filaments of wormlike micellar solutions.

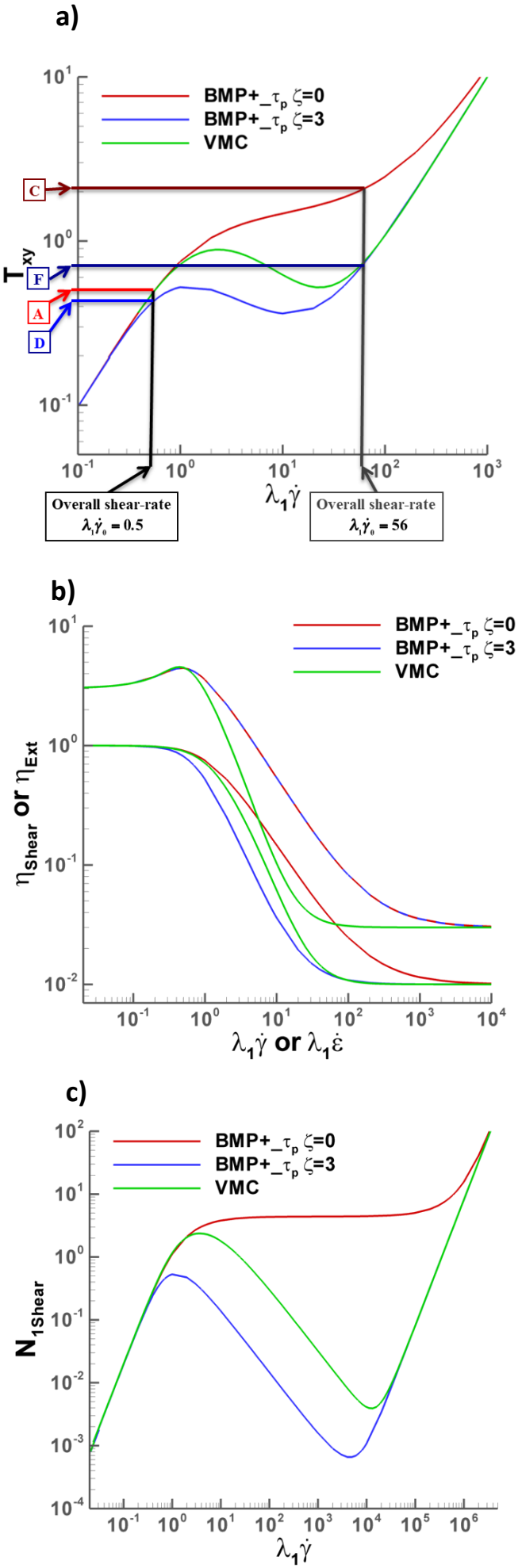

Figure 2. a) T_{rz} , b) *viscosity*, and c) N_{1Shear} against deformation-rate (simple shear & uniaxial extension); β=10^{-2}; BMP+_τ_p: {ω, ξ_{G0}, ξ, δ}={4, 0.1136, 2.27x10^{-7}, 1x10^{-6}}, non-shear-banding fluid (ζ=0), shear-banding fluid (ζ=3); VCM: {C_{Aeq}, C_{Beq}, ξ, ε, μ}={0.5, 0.7, 0.42, 7.5x10^{-7}, 1.5}.

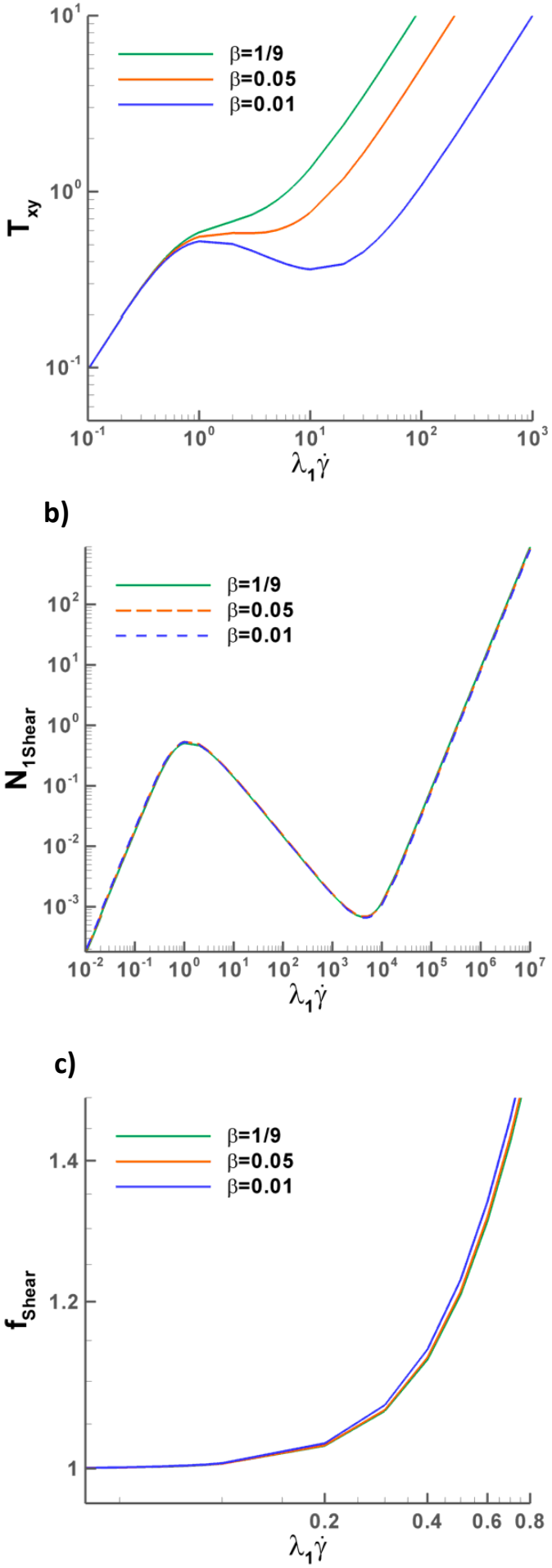

Figure 3. a) T_{xy}, b) N_{1Shear} and c) f against shear-rate (simple shear flow); BMP+_τ_p; $\{\omega, \xi_{G0}, \xi, \delta\}=\{4, 0.1136, 2.27\text{x}10^{-7}, 1\text{x}10^{-6}\}$; shear-banding fluid ($\zeta$=3)

To explore the various disparate regimes of segregated and non-segregated flow, *a choice of three key deformation-rates* $\lambda_1\dot{\gamma}_0$ (=*Wi*) has been made, counterpart to their equivalent global flow-rates. Therefore, the imposition of *Q*, and hence of *Wi*, implies an imposed target shear-rate in the flow-curve. Here, low ($\lambda_1\dot{\gamma}_0$=0.5, *Q*=4), intermediate ($\lambda_1\dot{\gamma}_0$=3.75, *Q*=30), high ($\lambda_1\dot{\gamma}_0$=56, *Q*=450) target shear-rates $\dot{\gamma}_0 (= U_{plate}/L)$ have been imposed. As shown in Table 1, each sampled deformation-rate then generates its associated flow-rate , which is applicable over the entire flow domain. Supporting flow profiles for these shear-rate levels are tested on two candidate fluids*: one fluid*, incapable of supporting flow-segregation (with ζ=0); and a *second fluid*, prone to generate shear-bands (with ζ=3). The (ζ=3)-fluid may manifest shear-bands in an intermediate shear-rate interval of $1 \leq \lambda_1\dot{\gamma}_0 \leq 10$ (Fig.2a). The stated combination of three key shear-rates and two fluids provides six instances to analyse and compare, as recorded in Table 1 and Fig.2a.

C. Flow domain, boundary conditions, ABS-f and centreline VGR-corrections, and *fe-fv* scheme

The flow problem is a modified Couette flow (Fig.3), where the dragging motion of an upper-plate promotes the flow through a planar contraction-expansion geometry. The obstruction has rounded-corners and the contraction aspect-ratio is α=4. As such, fully-developed steady simple-shear Couette flow is observed in regions away from the constriction, while inhomogeneous shear-to-extensional mixed flow prevails in the constriction-zone.

This modified plane Couette flow has been devised to provide a means of comparison between simple shear flow (in locations away from the contraction) and complex shear-to-extensional flow in the contraction region. Furthermore, in the inlet flow-region prior to the constriction, simple shear flow is maintained in the form of a traditional sliding-plate planar Couette flow (as observed in drag flows in co-axial cylinder and cone-and-plate rheometers).[3-6] In contrast, in the contraction zone, mixed shear-to-extensional deformation prevails, and its effects on the fluid-structure are evaluated. There, the simple shear flow is lost due to the presence of the constriction, and yet is recovered downstream of the constriction, where the condition of simple shear flow are re-established. Such a flow configuration can be found in many industrial devises, such as an extruder, where a molten polymer is carried by blades through an extruder screw, and then pushed through a dye (traditionally studied as a contraction flow), before being shaped or prepared for further processing.[36]

Periodic boundary condition strategies - banding against non-banding conditions

On the geometry-walls, pure-shear flow prevails, and the so-called no-slip boundary condition is assumed ($\boldsymbol{u} = \boldsymbol{0}$). Linear *velocity* u_x-profiles are specified at the geometry entry-exit, either as piece-wise linear for banding fluids or a single linear for non-banding fluid,

respectively. The profiles are determined based on the deformation-rate dictated by the flow-curve under the sampled shear-rate ($\dot{\gamma}_0 = U_{plate}/L$). Particularly important for stability at high deformation-rates, fully-developed entry and exit velocity-gradient ($\nabla \boldsymbol{u}$) are observed through feed-back/feed-forward procedures, as discussed in López-Aguilar et al.,[37-38]. *Stress* ($\boldsymbol{\tau}_p$) is not specified at outlet; hence, the stress is not periodic. In both banding and non-banding scenarios, it is only necessity to set the *pressure P* at flow-inlet, to impose a pressure level and remove pressure indeterminacy (flow exit attracts Dirichlet setting on velocity). Recall that different constant pressure-levels are recorded across upstream and downstream locations. This difference is caused by the presence of the constriction. Consistently, corresponding upstream and downstream fully-developed pressure-gradients are null. In practice, it has been found to be more appropriate to specify a pressure level at the inlet, thus avoiding the appearance of any false numerical artefacts in the inlet zone near the wall.

For banding instances:

(i) On velocity profiles, penetration into the field upstream is ensured, from entry to fully-developed zone, as well as in the downstream field. This ensures periodicity of the banding flow.

(ii) Since the velocity-gradient, stress and *f*-structure-function are discontinuous under banding and represented by step-functions across the banded-velocity zones, it is appropriate to take this into account in the discretisation. Starting from continuously extracted solutions, this can be achieved by a series of deferred-correction procedures, which involve incorporating *shock-capturing techniques* (*SCP*) to accurately resolve selected variables within each band. Hence, one may appeal to periodic analytic values (constants per band) and use them to iteratively correct *fe/fv* nodal values throughout the time-steps, within the fully-developed flow zones, as and where appropriate. One observes that the interface location between bands generally lies within the control volumes used, so that unique nodal values may be prescribed based on nodal allocation within a specific band.

Hybrid finite-element/finite-volume scheme

The numerical method employed is a hybrid finite-element/volume scheme as reported by López-Aguilar et al.[29-30] and references therein. In brief, this scheme is a semi-implicit, time-splitting, fractional three-staged formulation, which invokes finite-element (*fe*) discretisation for velocity-pressure (Q2-Q1, parent-cell) discretisation and cell-vertex finite-volume (*fv,* subcell) discretisation for stress. Together, the individual advantages and benefits of both the (*fe*) and (*fv*) approximation are combined. The sub-cell *fv*-triangular-tessellation is constructed within the parent *fe*-grid by connecting the mid-side nodes. Within such a structured tessellation, stress variables are located at the vertices of *fv*-sub-cells (offering linear interpolation) and solution projection is circumvented. In addition, Galerkin *fe*-discretisation is enforced on the embedded Navier-Stokes component-system. The fractional three-staged formulation consists of the momentum equation in stage-1, the pressure-

correction equation in stage-2 and the satisfaction of the incompressibility constraint in stage-3 (to ensure higher order precision). On solvers, this leads to a space-efficient element-by-element Jacobi iteration for stages 1 and 3; whereas for the pressure-correction stage 2, a direct Choleski solution method is utilised. At stage 1 of the stress solution , the discretisation using *fv* method results in a system that is diagonalised by design, which is immediately amenable to direct solution.

In order to attain numerical solutions under the present highly non-linear flow situations (recall β=10^{-2} and high *Q*-requirements), the absolute form for the internal-structure functional *f* (termed *ABS-f*-correction) is demanded within the implementation of the constitutive equation. The ABS-*f* correction arose as a physical argument to ensure thermodynamic consistency, with base on the Second Law of Thermodynamics. This correction poses an absolute-value constraint on each term contributing additively to the dissipation-function $\left|\boldsymbol{\tau}_p : \boldsymbol{D}\right|$ in Eq.(1), and enhances numerical tractability by enforcing consistent material property estimation.[37] Recovered velocity-gradients, denoted as a VGR-correction, are also required to achieve stable numerical solutions over wide ranges of deformation rate, ensuring discrete continuity imposition throughout the flow field.[37] Another consequence of the use of the ABS-*f* and VGR-corrections is the conspicuous increase of the level of non-linearity in which numerical algorithms loose tractability, traditionally denoted as a critical Weissenberg number Wi_{crit}. López-Aguilar et al.[37-38] recorded Wi_{crit}-increments of $O(10^3)$ on solutions obtained using the ABS-*f*/VGR doublet, with respect to simulations devoid of such corrections. Moreover, the ABS-*f* correction has been found to be generally applicable to other families of constitutive equations such as PTT and FENE.[37-38]

López-Aguilar et al.[38] recently reported on mesh characteristics and a mesh refinement study for 4:1:4 planar contraction-expansion with rounded edges geometry (Fig1.), as well as rheological equations of state in the Bautista-Manero family and solution algorithm. To complement such mesh-independence information with the problem to hand, BMP+_τ_p solutions captured in the fully-developed flow regions in the banding regime are illustrated in Fig.4. Here, node-element density is increased in the velocity-gradient direction, where construction of the coarse and the refined meshes display half and twice the number of elements, respectively, that the medium mesh has cross stream. The solution-capture test is performed in terms of the banded shear and normal stress profiles, as well as the location of the band interface. The chosen fluid is Case-E, capable to displaying banding under parametrisation $\{\beta, \omega, \xi_{G0}, \xi, \delta\}$=$\{10^{-2}$, 4, 0.1136, $2.27\text{x}10^{-7}$, $1\text{x}10^{-6}\}$. In general, solutions appear well-resolved as the location of the band-interface remains invariant across mesh densification. The medium and refined solutions approximate the interface location well, which was found to be at y_{int}~3.4 units for the test case. The normal and shear stress profiles have similar shapes and intensities, particularly on the refinement step from medium to refined. However, some localised noise is noted near the interface. This noise is due to the discontinuity posed by the interface and solution approximation. This is dealt with via a

shock-capture implementation, which is discussed in detail in the results section. Hence, from this point on, the medium mesh is considered for the solution description.

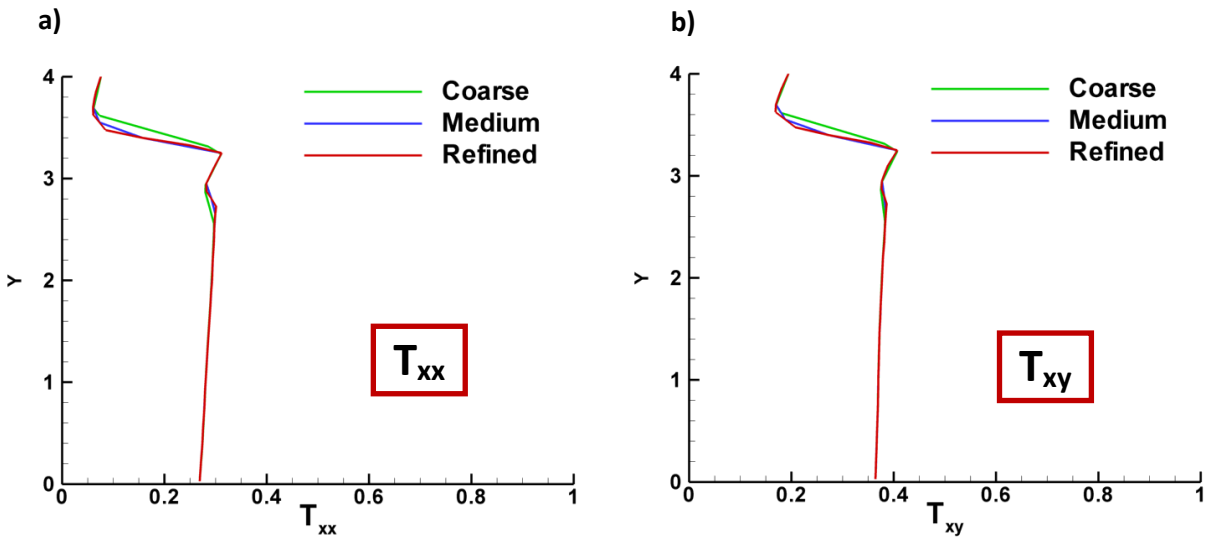

Figure 4. a) Normal-stress T_{xx} and b) shear-stress T_{xy} profiles sampled at the upstream fully-developed region; β=10^{-2}, {ω, ξ_{G0}, ξ, δ}={4, 0.1136, 2.27x10^{-7}, 1x10^{-6}}; mesh-refinement study for coarse, medium and refined grids; Case E: shear-banding fluid (ζ=3)

III. Numerical Predictions

In this section, the solutions for the cases in Table 1 demonstrate the ability of our BMP+_τ_p constitutive model and our numerical algorithm to generate banded or non-banded flows in the fully-develop region away from the constriction. These solutions also illustrate the influence of the obstruction and its mixed shear-to-extensional deformation fields on the attained flow-structure.

Particularly for the (ζ=3) banding-fluid, an intermediate flow-rate (Q=30) lies within the shear-banding deformation-rate range, making of banded-solutions possible. The lowest (Q=4) and highest (Q=450) flow-rates lie outside the shear-banding regime, where non-banded solutions are expected. In the following sections, details on the development of these instances are provided.

A. Banded against Non-banded solutions – Intermediate target flow-rate ($\lambda_1\dot{\gamma}_0$ =3.75), shear-banding fluid Case-E against non-shear-banding fluid Case-B

***Case-E Banded* velocity-u_x and structure (viscosity and structure-parameter-f) fields and profiles**

First, the ζ=3-banded Case-E is considered (Table 1), for which the corresponding velocity u_x-field is presented in Fig.5a. The nature of this complex planar-flow reveals simple shear-flow away from the contraction, and a combined shear-to-extensional deformation in the contraction-region. As such, several key-features may be observed and discerned from these two deformation states. In the upstream and downstream *fully-developed flow-regions*, one can observe a banded steady-state velocity u_x-field, with velocity-bands appearing in the

vertical *y*-spatial direction. The banded flow-pattern is then lost as the fluid approaches the constriction. Subsequently, one notes that, after traversing through the constriction and upon recovering simple-shear deformation, a banded fully-developed flow pattern is recovered.

In Fig.6a, flow-segregation is recorded through a split u_x-profile. This is sampled cross-stream at a fixed horizontal *x*-spatial coordinate in the upstream fully-developed flow region (one notes the null transversal velocity u_y-profile in Fig.6b).

The interface between bands is located at the inflection-point of such a split u_x-profile (y_{int}~3.48 units), where there is a sharp-change in colour-intensity in the fields (Fig.5a). Such an interface can be determined using the lever-rule,[6,31] to lie at a location of: $y_{int} = \left[\left(\dot{\gamma}_2 - \dot{\gamma}_0\right)/\left(\dot{\gamma}_2 - \dot{\gamma}_1\right)\right]\alpha_d$, where $\dot{\gamma}_0$ is the target characteristic shear-rate and α_d=4 units is the distance that separates the moving-plate and the contraction-wall.[**] As such, $\dot{\gamma}_0$=3.75 and T_{xy}~0.4 units (Fig.7a), in this case, it is located in the unstable non-monotonic shear-stress regime. Then, extracted from the flow curve at an equivalent shear-stress level T_{xy}~0.4 units, $\dot{\gamma}_1$ =0.6 units and $\dot{\gamma}_2$ =27 units are the low and high shear-rate stable-branches, respectively. Each band, which constitutes the split u_x-profile, is then supported by its corresponding shear-rate, with the low-$\dot{\gamma}_1$ and high-$\dot{\gamma}_2$ shear-rates being assigned to the lower and upper bands, respectively. Then, the narrow upper-band in the local neighbourhood of the moving-plate (with a red/intense-core; Fig.5a) represents the material in the high-$\dot{\gamma}_2$ shear-rate band. In terms of rheological response (Fig.7b), this high-$\dot{\gamma}_2$ shear-rate band corresponds to a highly-unstructured fluid of total-viscosity η_{Tot}~1.8x10^{-2} units (see blue band in viscosity field in Fig.5c and counterpart red-fringe in the structure-parameter *f*-field of Fig.5d). In contrast, the low-$\dot{\gamma}_1$ shear-rate band occupies the remaining channel-space, lying between the band-interface and the bottom geometry-wall (homogeneous blue band in *f*-field of Fig.5d). Here, a highly-structured fluid is reported, with a viscosity of η_{Tot}~0.8 units (as indicated by the orange band in viscosity field in Fig.5c).

In the *complex flow region*, the pre-banded flow field is disrupted and distorted by the constriction, with unstructured material flowing through the constriction-gap, while highly-structured material occupies the stagnant corners (as shown in the viscosity field representation, Fig.5c). In Fig.6d, the cross-stream velocity U_x-profile in the contraction gap displays changes of slope near the contraction and top walls, fact that reflects the non-homogeneity of the flow in the contraction-region. Then, beyond the constriction, and once the fluid-viscosity has had the opportunity to readjust, a banded morphology is reformed (nb. the downstream intermediate-green viscosity colour levels, illustrate convection downstream).

A clarification is worthwhile regarding the meaning of the terms ‘inhomogeneous deformation’ and ‘inhomogeneous flow’ for the rheological community. In complex flows studied under the umbrella of non-Newtonian fluid mechanics, ‘inhomogeneous flow/deformation’ refers to a flow in which simultaneous shear and extensional deformations are mixed in the domain. In contrast, in rheometry, where shear-banding has traditionally been studied, an ‘inhomogeneous field’ refers to field with fluid segregation (bands) in a

[**] α_d=4 also corresponds to the contraction ratio (α) in this contraction-expansion geometry.

simple shear deformation. Hence, in this paper, to address this issue, we differentiate and define the concept of ‘complex flow’ as a mixed inhomogeneous shear-to-extensional deformation. Additionally, we define ‘banded flow’ as a flow that supports the coexistence of two bands of material with different physical properties, i.e. viscosity.

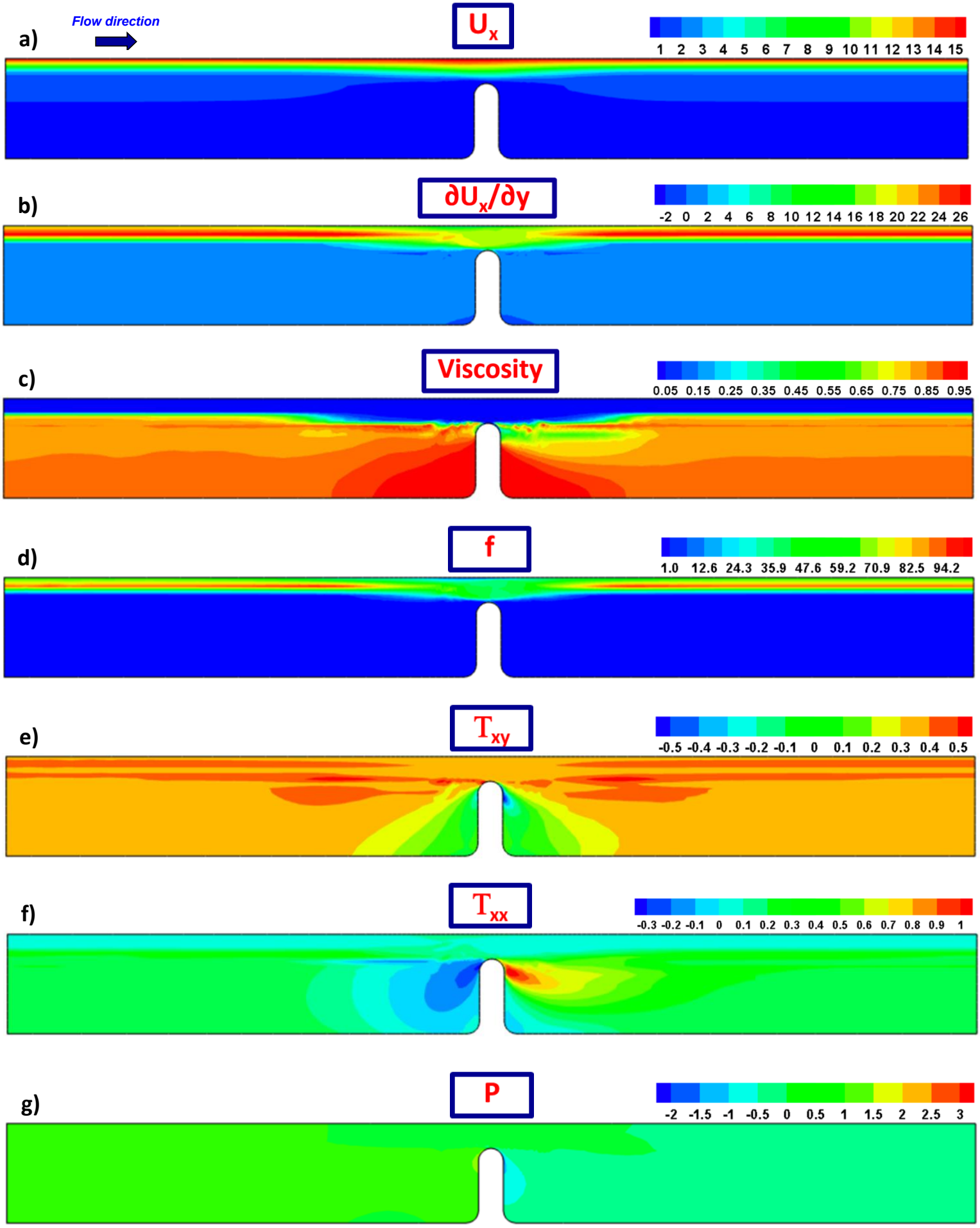

Figure 5. a) Velocity U_x , b) shear-rate $\partial U_x/\partial$y, c) viscosity, d) *f*-functional, e) shear-stress T_{xy}, f) normal-stress T_{xx} and g) pressure *P* fields; β=10^{-2}, {ω, ξ_{G0}, ξ, δ}={4, 0.1136, 2.27x10^{-7}, 1x10^{-6}}; Case E: shear-banding fluid (ζ=3)

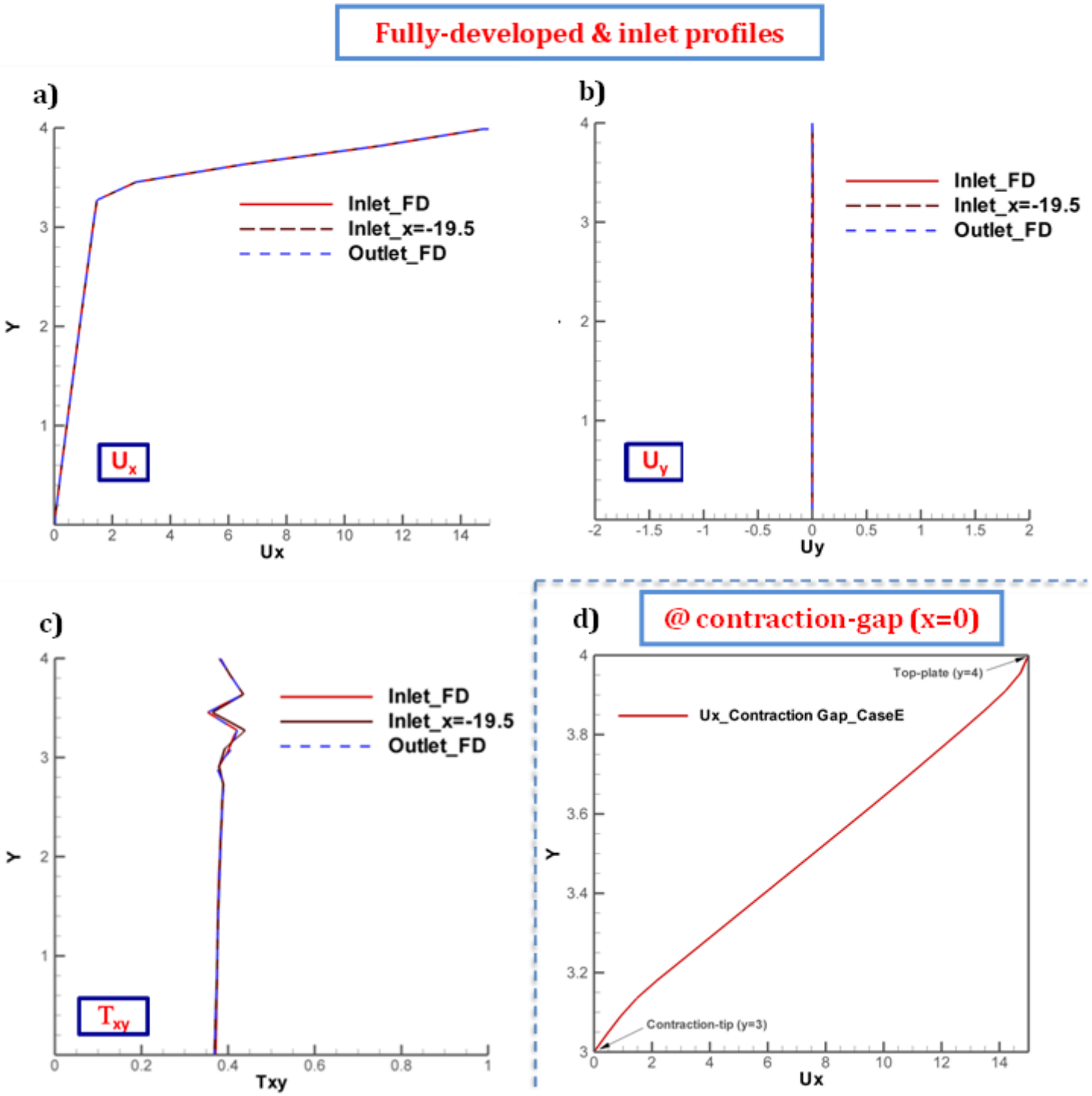

Figure 6. Profiles of a) U_x b) U_y , c) T_{xy} and d) U_x @ contraction-gap;
β=10^{-2}, {ω, ξ_{G0}, ξ, δ}={4, 0.1136, 2.27x10^{-7}, 1x10^{-6}}; Case E: shear-banding fluid (ζ=3)

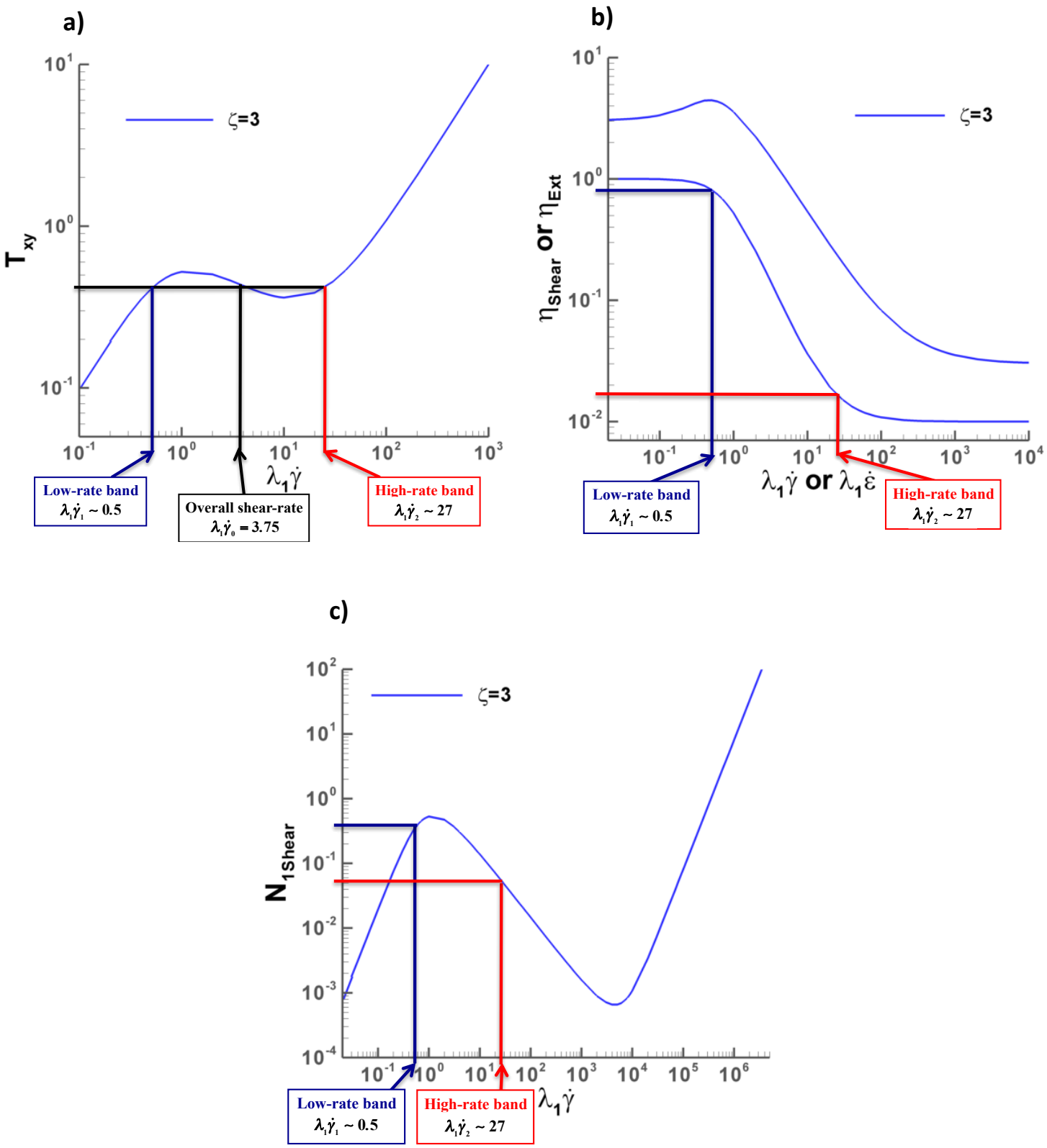

Figure 7. a) T_{rz} , b) η_{Shear} and η_{Ext}, and c) N_{1Shear} against deformation-rate (simple shear & uniaxial extension); BMP+_τ_p; β=10^{-2}, {ω, ξ_{G0}, ξ, δ}={4, 0.1136, 2.27x10^{-7}, 1x10^{-6}}; Case E: shear-banding fluid (ζ=3)

Case-E banded shear and normal stress fields and profiles, and pressure-field

The fully-developed banded velocity-profile response of ζ=3-solution is accompanied by a roughly constant shear-stress T_{xy}-field (Fig.5e). Notably, at the channel-height where the interface between the bands appears, a horizontal strip of slightly larger T_{xy}-values is apparent. The counterpart T_{xy}-profile reveals a constant T_{xy}-level (~0.4 units; Fig.6c), which appears throughout the flow-gap. Precisely near the interface location, the T_{xy}-profile oscillates about the mean level. This is consistent with the discretisation and the discontinuous nature of the shear-rate profile across the flow-gap, which ideally necessitates *shock-capturing techniques* for more accurate resolution (see earlier remarks). These undulations coincide with the slightly more intense strips observed and may be associated with the discontinuity posed by the interface (see on with *shock-capturing*). Conspicuously, the normal-stress T_{xx} also inherits bands, driven by the velocity profile (Fig.5f). Such banding in normal-stress components has also been observed in non-extensional large amplitude oscillatory shear (LAOS) predictions using the Rolie-Poly model.[39] Once more, the homogeneous T_{xy}-field and the inhomogeneous T_{xx}-response in the fully-developed regions are disturbed by the presence of the constriction (Fig.5e-f). Here, the effects of the combined shear-extensional deformation are more evident. On T_{xy}, the stripped-interface disappears and a homogeneous T_{xy}-level is adopted in the constriction-gap (Fig.5e). Moreover, in the recess-zones, there are triangular green-structures, and a localised small blue-zone emerges on the contraction back-face, near its tip. Consistently, on T_{xx}, two coloured-level regions are reported; with base on the contraction-tip of negative-blue values upstream and a positive-red counterpart downstream (Fig.5f).

In Case E, the pressure sustaining flow passes from a green-uniform base-pressure-level to a relatively lower and brighter-green pressure-level downstream of the contraction (Fig.5g, $P_{outlet}/(1+P_{inlet})\sim5x10^{-1}$). Note that in the upstream and downstream fully-developed regions, pressure-fields appear independent of the main-flow x-direction, consistent with Couette-deformation. The upstream-to-downstream pressure-level adjustment is provoked by the mixed shear-to-extension flow within the constriction.

From such a continuous solution representation, deferred-correction solutions may be considered when incorporating *shock-capturing (SCP)* across the bands to more directly address solution-discontinuity and its localisation. The effectiveness of this strategy may be demonstrated by comparing cross-stream profiles of solution refinements with *no-shock-capturing* solutions. Here, the entry SCP-conditions are set as analytic in velocity-gradient and stress, which imposes the f-structure-function (Fig.8). The exit SCP-conditions are then taken as follows: first by imposing periodicity on the f-structure-function; secondly, by imposing periodicity on velocity-gradients; thirdly, by imposing periodicity on both; Then, stress is computed as before. The corresponding exit-flow SCP-solutions are provided in Fig.9, for both major stress components (T_{xy}, T_{xx}). Through these solutions, one can contrast the analytic entry SCP-conditions. Here, the major correction influence is from periodicity in

the velocity-gradients. Any correction from the *f*-structure-function (alone/in combination with velocity gradients) is seen to deteriorate the quality of exit-stress profiles. In this data, the overall quality of the none-shock-captured solution is also complemented.

Case-B Non-banded **Velocity field**

For Case-*B* (non-shear-banding fluid ζ=0; Table 1 and Fig.10) and in contrast to Case-*E* (ζ=3, Fig.5), the fully-developed velocity u_x-field now appears as a single and continuous shear-rate form, as shown in Fig.10a-b. This is accompanied by upstream-downstream constant non-segregated T_{xy}- and T_{xx}-levels Fig.10e-f. Such a linear upstream velocity-profile is lost in the constriction zone, where the fluid is accelerated as a consequence of the converging flow. Here, the T_{xy}-field develops strongly positive and negative localised regions attached to the contraction walls, and a negative elongated region on the moving-plate (Fig.10e). The normal stress T_{xx}-field presents a strong elastic-zone in the contraction-region (Fig.10f), followed stream-wise by a negative zone whose influence appears to be convected downstream. In the upstream recess zone, there is an additional negative-strong patch, which is balanced downstream by an isolated red-positive core that elongates into a tail downstream.

In terms of fluid-structure and away from the constriction-zone, the viscosity (and its counterpart structure-parameter-*f*) distribution remains at a single constant-level upstream (Fig.10c-d). Then, as the fluid approaches the contraction, the varied and distributed deformation-rate breaks down its structure, resulting an asymmetric blue low-viscosity region filling the constriction. In the deceleration zone beyond the constriction, the material is observed to recover its structure. This fact is witnessed, via the viscosity-field, by a sudden change from a highly-unstructured fluid (blue), to a more structured fluid (green). This is expressed through two elongated arms directed downstream, one sticking to the moving-plate and the other located in the middle of the domain.

In the recess-zones, there are isolated red/high-viscosity triangular-shaped zones, suggesting relatively slow motion in these vicinities. Here, due to the highly-nonlinear conditions based on polymer-content (β=10^{-2}) and increased flow-rate, the pressure-drop required to drive the flow is enforced through a fixed-pressure boundary-condition at the inlet. This implies that the resulting pressure level must be calculated at the flow-outlet. Such a procedure ensures that no downstream blockage is created in pressure, which may otherwise degrade the downstream solution quality in taking up fully-developed flow conditions. The ensuing *pressure* field passes from one of a characteristic constant-pressure Couette flow upstream (Fig.10f) to a similar form downstream. Afterwards, a pressure build-up (pressure-gradient, ~19.9 units) sustains the flow through the constriction.

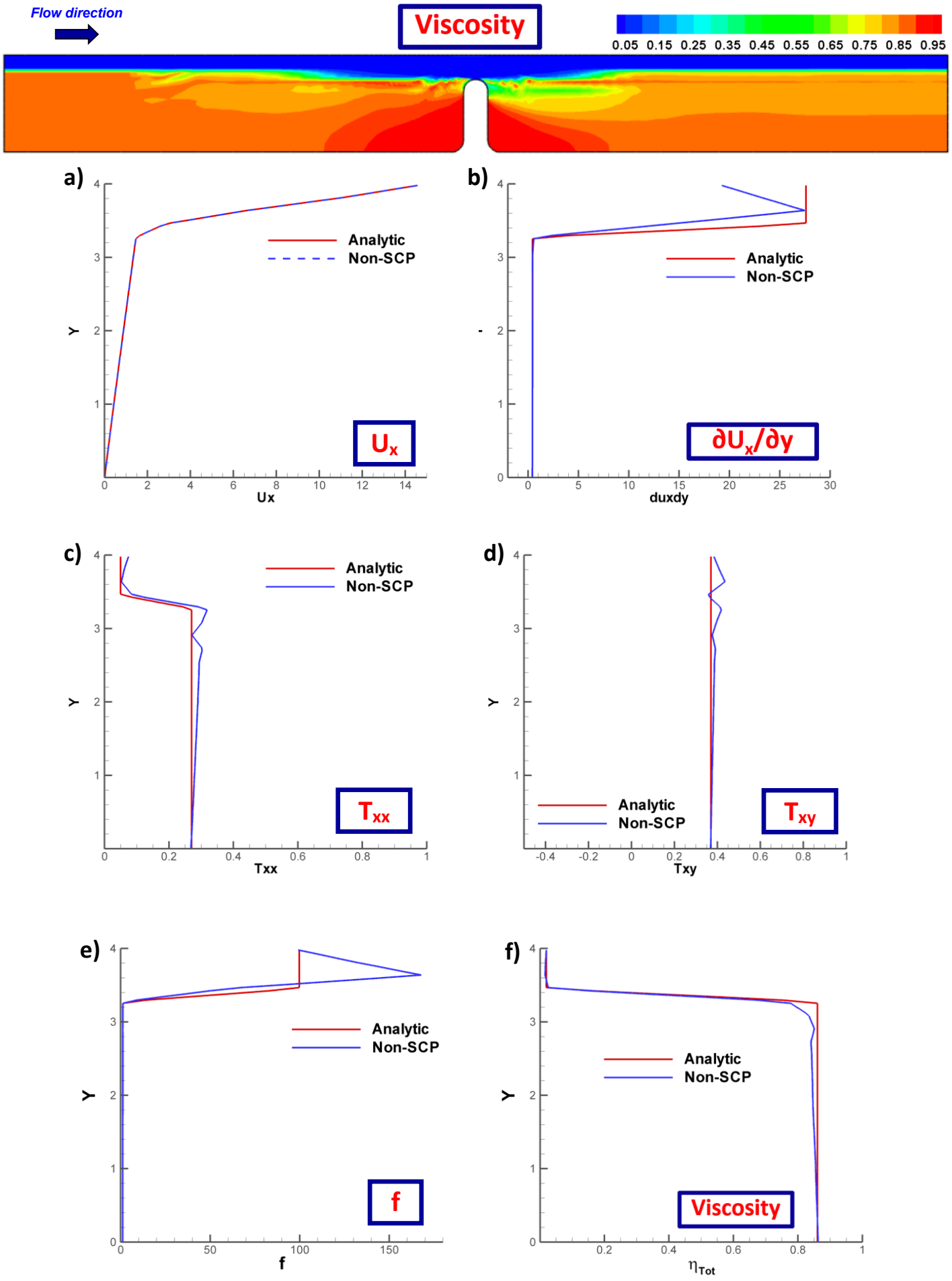

Figure 8. Banded-solution profiles: entry-analytic vs exit-Non-SCP; a) velocity U_x , b) shear-rate $\partial U_x/\partial y$, c) normal-stress T_{xx}, d) shear-stress T_{xy}, e) f-functional, f) viscosity;
BMP+_τ_p; β=0.01, {ω, ξ_{G0}, ξ, δ}={4, 0.1136, 2.27x10^{-7}, 1x10^{-6}}; Case E: shear-banding fluid (ζ=3)

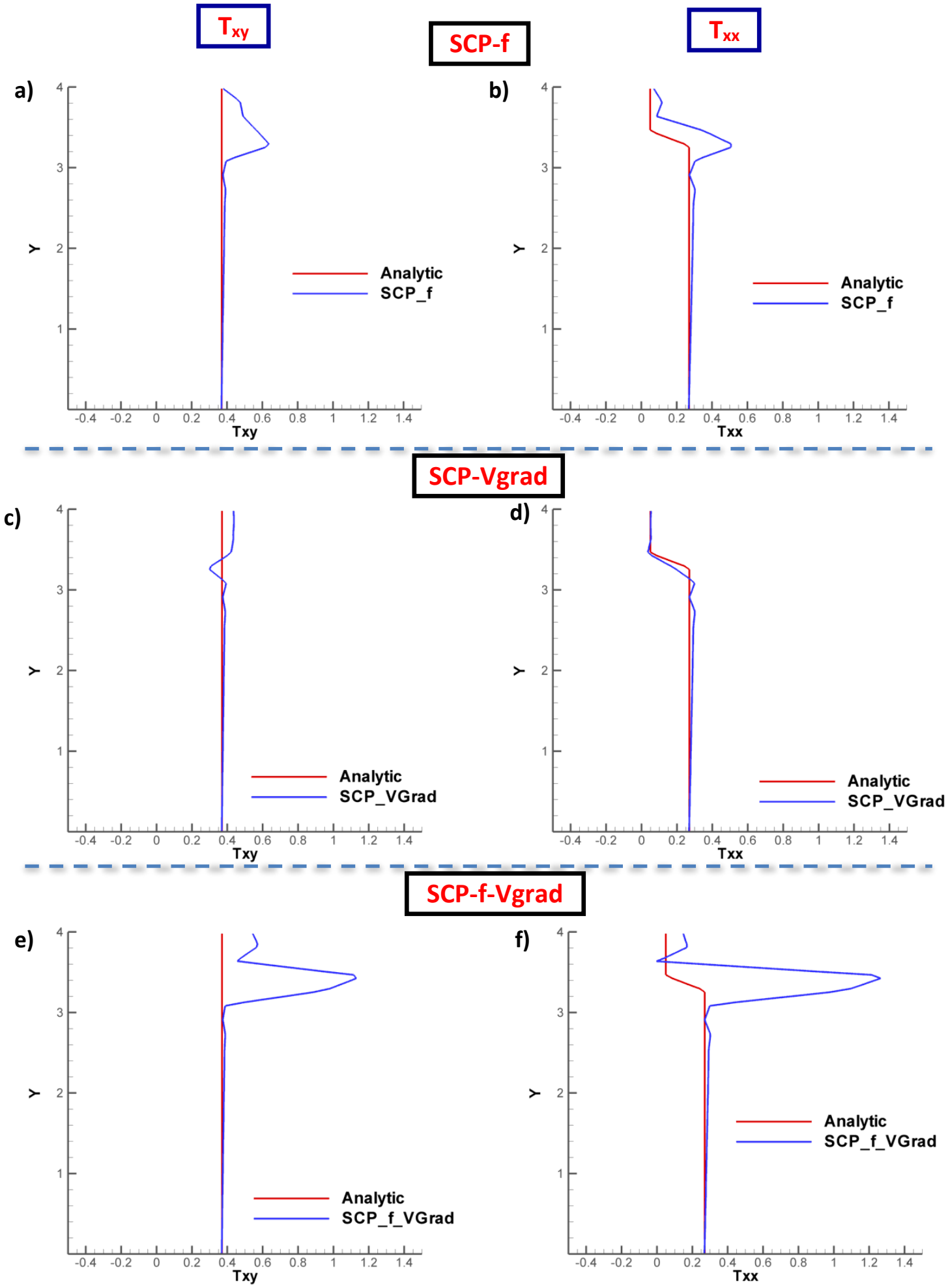

Figure 9. Banded-solution profiles under shock captures (SCP): analytic-entry vs exit-SCP; SCP-f: a) shear-stress T_{xy}, b) normal-stress T_{xx}; SCP-Vgrad: c) T_{xy}, d) T_{xx}; SCP-f-Vgrad: e) T_{xy}, f) T_{xx}; BMP+_τ_p; β=0.01, $\{\omega, \xi_{G0}, \xi, \delta\}$={4, 0.1136, 2.27x10^{-7}, 1x10^{-6}}; Case E: shear-banding fluid (ζ=3)

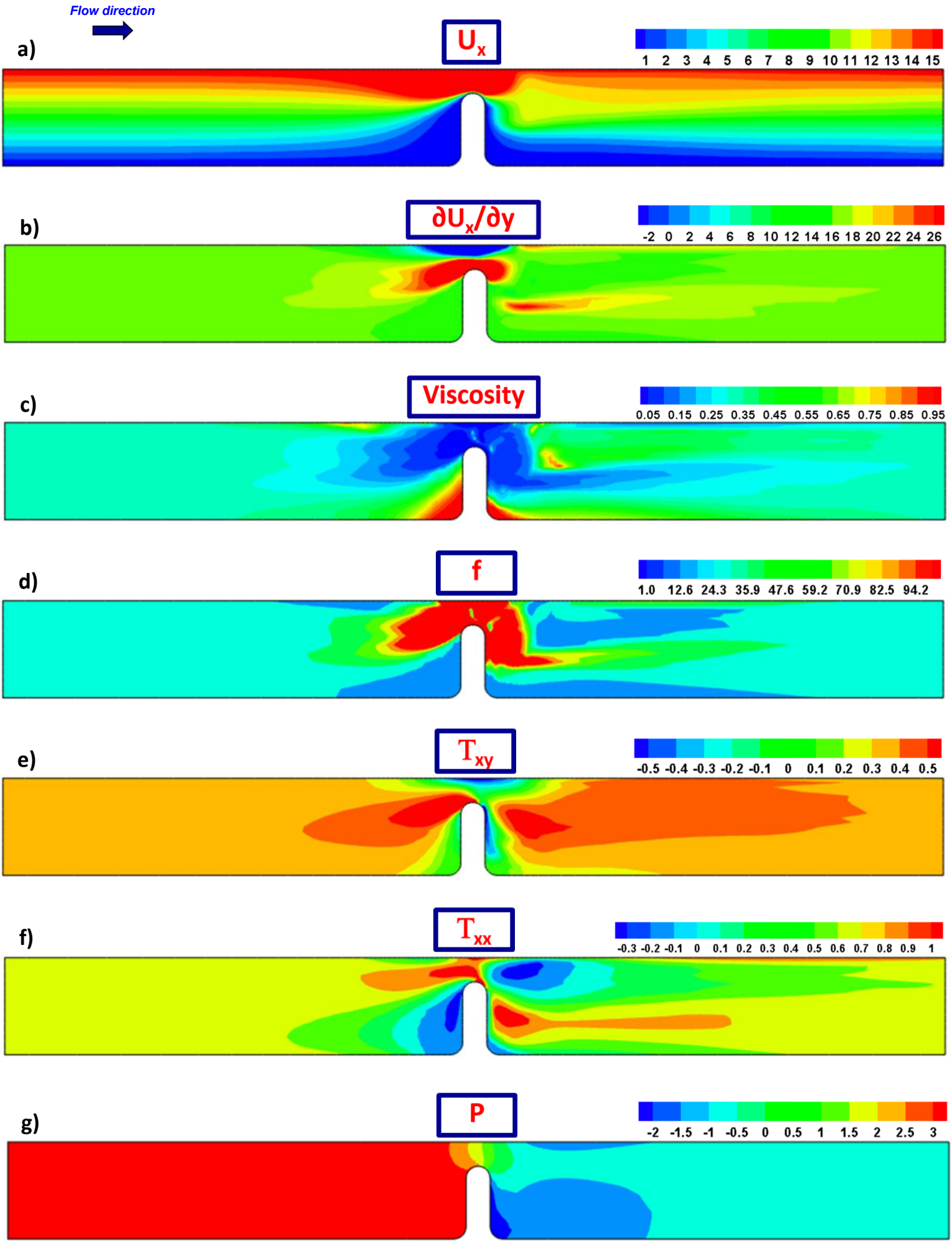

Figure 10. a) Velocity U_x , b) shear-rate $\partial U_x/\partial$y, c) viscosity, d) f-functional, e) shear-stress T_{xy}, f) normal-stress T_{xx} and g) pressure P fields; β=10^{-2}, {ω, ξ_{G0}, ξ, δ}={4, 0.1136, 2.27x10^{-7}, 1x10^{-6}};
Case B: non-shear-banding fluid (ζ=0)

Considering low deformation-rates (Q=4; $\dot{\gamma}_0$=0.5) the instances of the shear-banding fluid (ζ=3; case-*D*), which lies outside the unstable branch of the flow-curve (Fig.11a-b), and the non-shear-banding fluid (ζ=0; case-*A*), the predictions indicate single-banded u_x-fields (Fig.12a-b). Across both instances (A and D), and at this relatively low state of deformation, solutions adopt a similar form, with only slight level-differences detected in the constriction-gap. In the *fully-developed regions*, the single-banded velocity profiles are supported by uniform states in T_{xy} and T_{xx} stress-fields (Fig.11e-f and Fig.12e-f, respectively). Notably, the shear-banding (ζ=3; case-*D*) fluid solution-set yields less intense features, with a single green-level apparent around the constriction-zone. Correspondingly, the non-shear-banding (ζ=0) case-*A* solution sustains intense stress-levels. These differences may be correlated with the relatively larger shear and normal stress levels for the non-shear-banding A-fluid (indicated in Fig.2a). Recall that non-zero shear-banding intensity parameters *$\zeta \neq 0$ provoke exaggerated shear-thinning* features (see shear rate differences Fig.11b and Fig.12b).

This low flow-rate (Q=4; $\dot{\gamma}_0$=0.5) has been chosen to impose a stable-branch deformation-rate in the flow-curve, while still maintaining some differences between shear-banding and non-shear-banding fluids. Here, for the shear-banding fluid (ζ=3), one can observe a slightly lower T_{xy}-level compared to the non-shear-banding (ζ=0)-case. This (ζ=3) decline in T_{xy} slope is related to the proximity to the flow-curve maxima at higher shear-rate levels.

In terms of fluid-structure, for case-*D* (ζ=3)-*viscosity* and *f*-fields (Fig.11c-d) reflect liquefied material in the constriction-zone, while it is fully-structured in the recess-zones (red-levels). The extremes in viscosity distribution noticeably spread and fill the constriction-zone (blue-levels), while relatively smaller viscosity-levels occupy the fully-developed regions (green-shading, Fig.11c-d). In contrast in Fig.12c-d, case-A (ζ=0)-viscosity-fields display a relatively structured material away from the constriction (red-levels) and isolated thinned-blue fluid patches that have base on the contraction-tip and the wall. They only influence the material from around the constriction-zone.

This distinct change in structural-behaviour can be attributed to the exaggerated shear-thinning properties of the shear-banding case-D (ζ=3) fluid. At a fixed shear-rate (beyond $\dot{\gamma}_0$ ~0.3), the shear-banding case-D (ζ=3) fluid produces a less-responsive system, with relatively lower levels of material-change than those of the non-shear-banding case-*A* (ζ=0) fluid. This can be observed from the rheology of the flow-curve in Fig.2a when comparing the field solutions of case-A and case-D. The only caveat to this statement lies in the pressure field, both around and downstream of the constriction, which is significantly more disrupted under the shear-banding case-D (ζ=3) fluid (Fig.11g) than for the non-shear-banding case-*A* (ζ=0) fluid (Fig.12g).

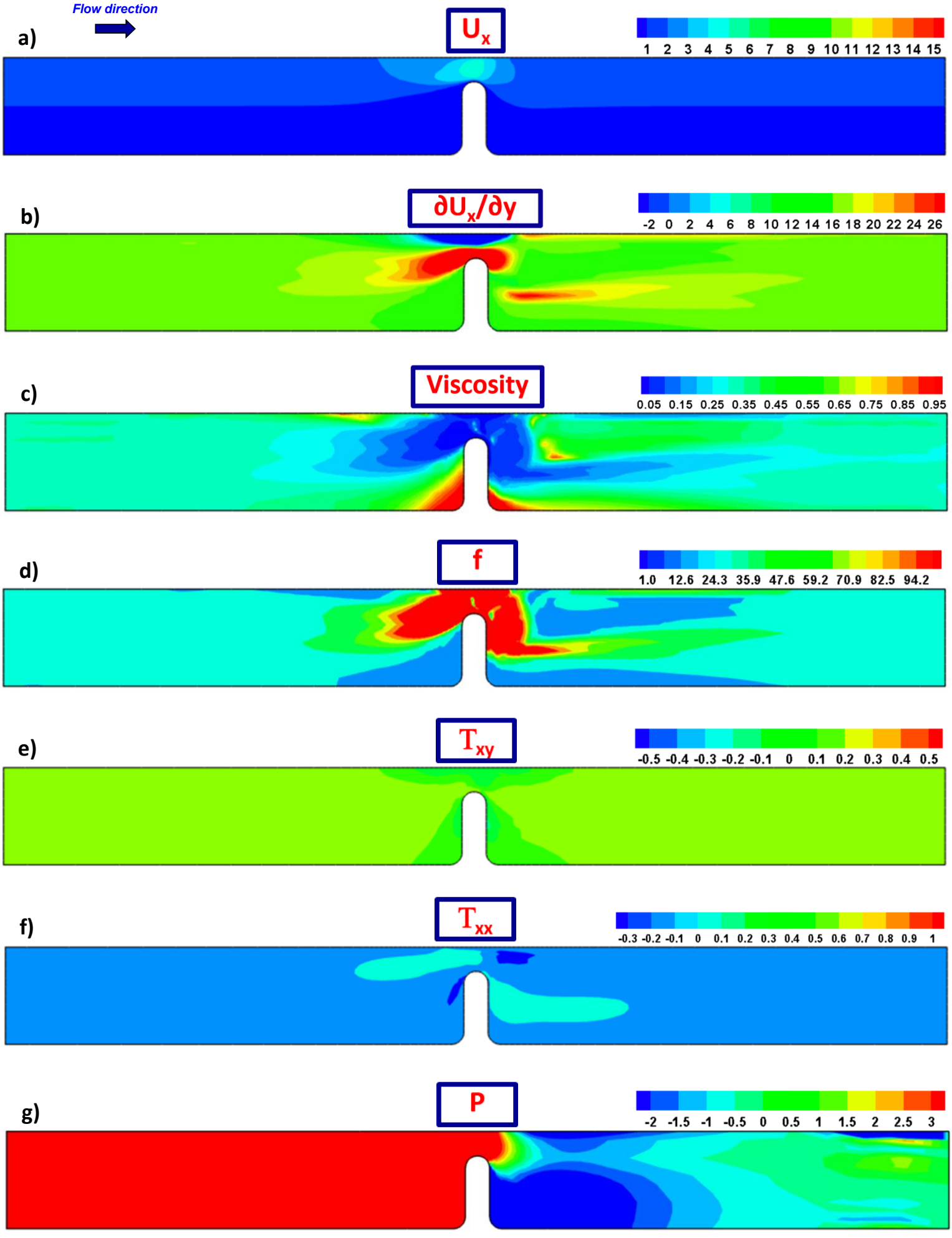

Figure 11. a) Velocity U_x , b) shear-rate $\partial U_x/\partial$y, c) viscosity, d) *f*-functional, e) shear-stress T_{xy}, f) normal-stress T_{xx} and g) pressure P fields; β=10^{-2}, {ω, ξ_{G0}, ξ, δ}={4, 0.1136, 2.27x10^{-7}, 1x10^{-6}};
Case D: shear-banding fluid (ζ=3)

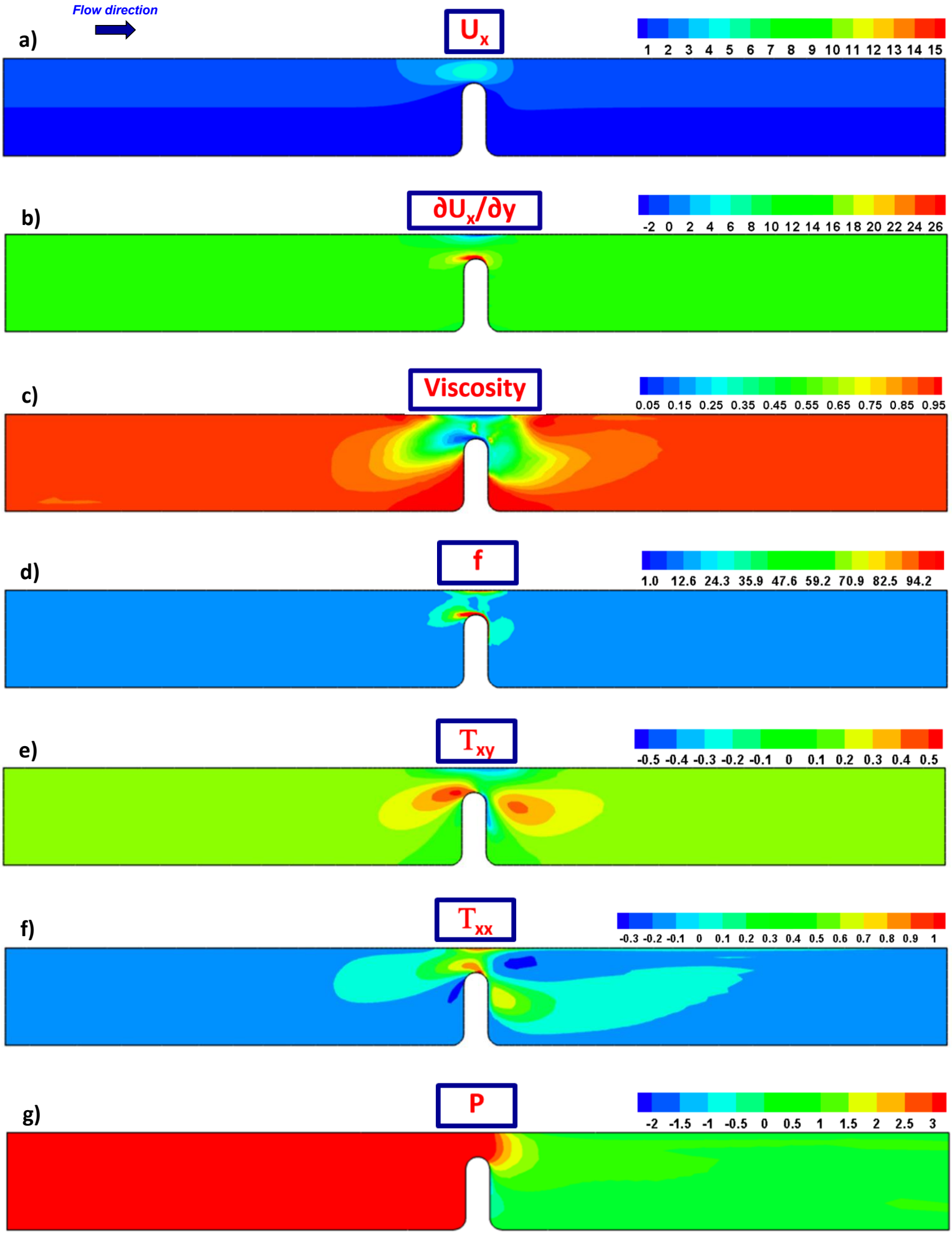

Figure 12. a) Velocity U_x , b) shear-rate $\partial U_x/\partial$y, c) viscosity, d) *f*-functional, e) shear-stress T_{xy}, f) normal-stress T_{xx} and g) pressure P fields; β=10^{-2}, {ω, ξ_{G0}, ξ, δ}={4, 0.1136, 2.27x10^{-7}, 1x10^{-6}};
Case A: non-shear-banding fluid (ζ=0)

***Case-C and Cased-F non-banded* solutions**

In the alternative extreme of high deformation-rate, the second stable-branch of the flow-curve is located, as shown by solutions at (Q=450; $\dot{\gamma}_0$=56) (Fig.2a). There, in the *non-shear-banding (ζ=0) case-C* solution (Fig.13), a strong single-banded u_x-field is captured away from the constriction. In the complex-flow constriction region, intense activity is recorded through stress T_{xy}- and T_{xx}-zones, which are based on the contraction-tip and around the moving-wall (Fig.13e-f). Here, the large velocity of the moving-wall causes increased kinematics stimulated to convect downstream the relatively-strong levels of stress from the constriction-zone. In this high deformation-rate instance, the fluid-viscosity drops dramatically, filling almost the entire geometry (Fig.13c-d). That is, with the exception of the recess-regions, which acquire structured material response and appear as reduced red-zones.

Unfortunately, in contrast, the *high-rate* shear-banding *(ζ=3) case-F* proved to be computationally intractable for conditions of severely-low solvent-fraction (β=10^{-2}). This is due to the combination of three key factors: the already extremely high flow-rate Q=450; the outstandingly-high polymer-content (1-β)=0.99; and the additional non-linearity invoked by the non-zero shear-banding intensity parameter ($\zeta\neq0$). Nevertheless, some evidence for the influence of ζ-increase may be drawn from solutions extracted in the reduced range $0.001\leq\zeta\leq0.03$, but at the larger permitting solvent-fraction β=1/9. One notes therefore, that a final and stable steady-state solution may be gathered computationally only for a (ζ=0.03)-fluid. Under these conditions, oscillations in normal-stress are observed, signalling pending intractability. This implies that this fluid is in its high deformation-rate stable branch of the T_{xy} flow-curve, while N_{1Shear} lies within its unstable branch. As these solutions do not significantly deviate from (ζ=0)–solutions, this data is withheld.

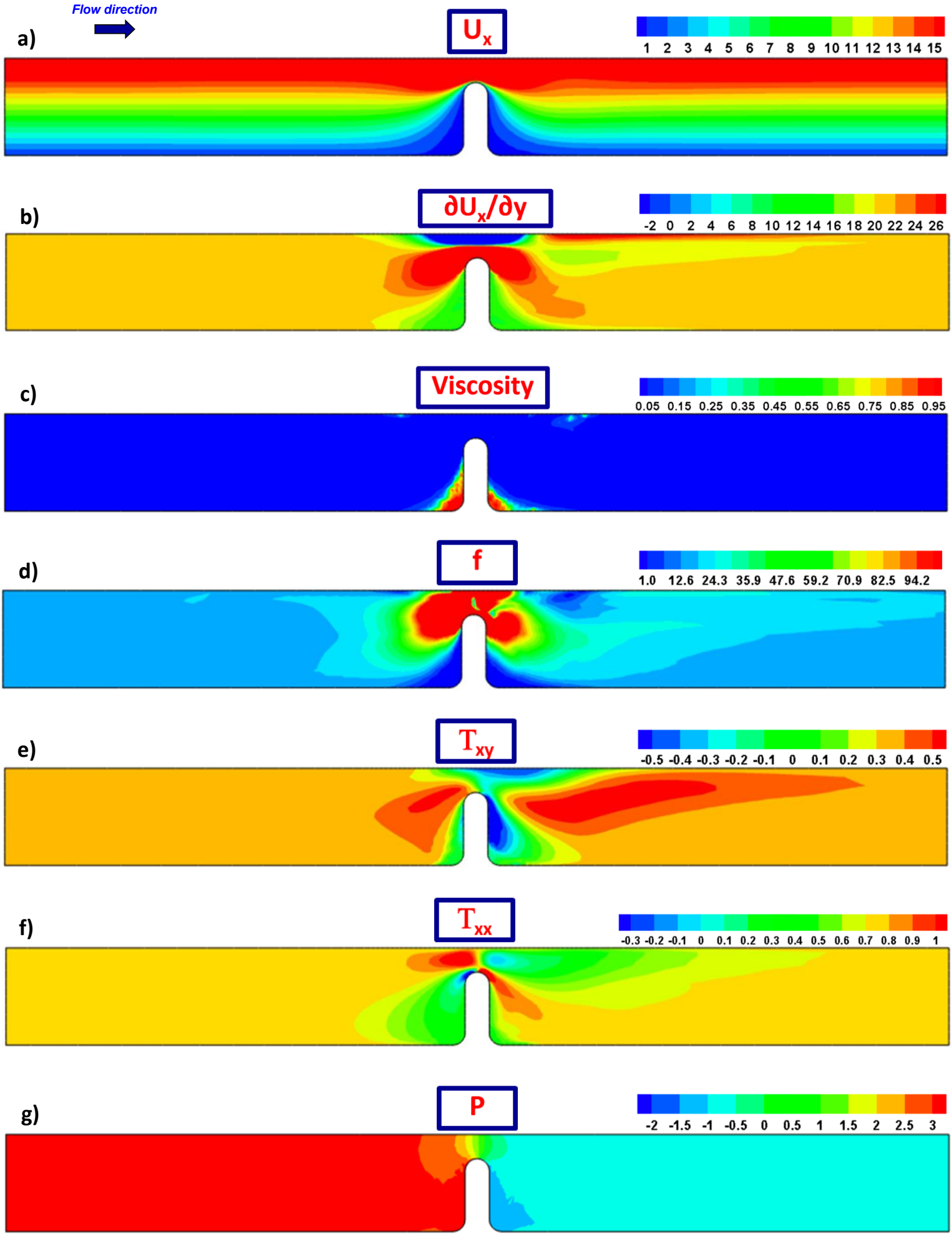

Figure 13. a) Velocity U_x , b) shear-rate $\partial U_x/\partial y$, c) viscosity, d) *f*-functional, e) shear-stress T_{xy}, f) normal stress T_{xx} and g) *P* fields;$\beta=10^{-2}$, $\{\omega, \xi_{G0}, \xi, \delta\}=\{4, 0.1136, 2.27\text{x}10^{-7}, 1\text{x}10^{-6}\}$; Case C: non-shear-banding fluid ($\zeta=0$)

IV. Conclusions

In this work, novel solutions are reported for the shear-banding of micellar systems in a complex modified planar Couette flow. Banded solutions have been attained using the BMP+_τ_p model to approximate the rheological response of highly-concentrated (solvent-fraction $\beta \leq 10^{-2}$) wormlike micellar solutions. In this manner, away from the constriction, simple shear-flow is observed, while inhomogeneous shear-to-extensional flow is gathered about the contraction.

To contrast banding against non-banding response, two fluid representations have been chosen: a shear-banding fluid (non-monotonic flow-curve with localised extrema) and a non-shear-banding fluid (monotonic flow-curve). Then, three overall flow-rates were fixed on the flow-curve, where each flow-rate corresponded to a low, intermediate and high shear-rate, respectively. Armed with these combinations, six independent instances were identified for study across two fluid-types (shear-banding/non-shear-banding) and three flow-rates (stable/unstable/stable).

The banding fluid in the intermediate flow-rate generates segregated flow-fields away from the contraction, represented via velocity, normal stress and flow structure (viscosity or fluidity). Cross-stream fully-developed samples reflect split velocity and normal-stress profiles, while shear-stress profiles appear constant. Such inhomogeneous response is lost in the contraction-zone, where flow-structure readjusts to the multiple and distributed rates encountered. This leads to a highly-unstructured material response that is accelerated and stretched due to the obstruction-blockage. Interestingly, pressure sustains a Couette-like form away from the contraction, with constant pressure-levels that vary from upstream-to-downstream due to the inhomogeneous shear-to-extensional flow posed by the constriction. One notes in particular is that downstream of the constriction, a banding fluid in an intermediate flow-rate regime, shows a tendency to resume banded profiles, having experienced the disorder of the flow around the constriction. The plausibility of banding in N_{1Shear} alone, and not within T_{xy}, is also considered an interesting and open issue to be resolved.

In contrast and apart from the region of contraction, the non-shear-banding fluid displays homogeneous velocity, shear-stress and normal-stress fields and profiles, indicating a relatively more structured material response. Flow instances in the stable branches of the flow-curves, at low and high flow-rates, consistently reflect simpler, non-segregated flow fields, with degrees of structure modulated by the individual deformation-rate imposed. Due to the high degree of non-linearity caused by the extremely high solute-concentration ($\beta \leq 10^{-2}$), the case of the banding fluid at high-Q is found to be numerically intractable. However, such predictive limitation may be addressed via larger-β solutions (β=1/9), under which normal-stress oscillations are observed as a signal of pending intractability. The implication here is that this fluid is in its high deformation-rate stable branch of the T_{xy} flow-curve, while N_{1Shear} lies within its unstable branch.

The findings presented in this manuscript suggest new avenues of research, such as the localisation in extensional deformation. This phenomenon is relevant to extension necking in wormlike micellar solutions,[9,10] contraction[15] and pipe flows.[40] Future studies will focus on these topics.

Acknowledgements

JELA acknowledges the support from Consejo Nacional de Ciencia y Tecnología (CONACYT, Mexico) and from Universidad Nacional Autónoma de México UNAM (grant numbers PAPIIT IA102022 and PAIP 5000-9172 Facultad de Química). JELA and OM acknowledge the support from UNAM under the project with grant number PAPIIT IN100623. HRTJ acknowledge the support of Prof. Nithiarasu, Associate Dean - Research, Innovation and Impact (RII), Faculty of Science and Engineering, Swansea University, UK

References

[1]V. J. Anderson, J. R. A. Pearson, and E. S. Boek, "The rheology of worm-like micellar fluids," Rheol. Rev. 217–253 (2006).

[2]M. E. Cates and S. M. Fielding, "Rheology of giant micelles," Adv. Phys. **55**, 799–879 (2006).

[3]P. D. Olmsted, "Perspectives on shear banding in complex fluids," Rheol. Acta **47**, 283–300 (2008).

[4]S. Manneville, "Recent experimental probes of shear banding," Rheol. Acta **47**, 301–318 (2008).

[5]G. Ovarlez, S. Rodts, X. Chateau, and P. Coussot, "Phenomenology and physical origin of shear localization and shear banding in complex fluids," Rheol. Acta **48**, 831–844 (2009).

[6]T. Divoux, M. A. Fardin, S. Manneville, S. Lerouge, "Shear banding of complex fluids," Annu. Rev. Fluid Mech. **48**, 81–103 (2016).

[7]J. R. A. Pearson, "Flow curves with a maximum," J. Rheol. **38**, 309–331 (1994).

[8]N. Germann, A. K. Gurnon, L. Zhou, L. P. Cook, A. N. Beris, and N. J. Wagner, "Validation of constitutive modeling of shear banding, threadlike wormlike micellar fluids," J. Rheol. **60**, 983–999 (2016).

[9]S. M. Fielding, "Triggers and signatures of shear banding in steady and time-dependent flows," J. Rheol. **60**, 821–834 (2016).

[10]M. Cromer, L. P. Cook, and G. H. McKinley, "Extensional flow of wormlike micellar solutions," Chem. Eng. Sci. **64**, 4588–4596 (2009).

[11]M. Cromer and L. P. Cook, "A study of pressure-driven flow of wormlike micellar solutions through a converging/diverging channel," J. Rheol. **60**, 953 (2016).

[12]J. E. López-Aguilar, M. F. Webster, H. R. Tamaddon-Jahromi, and O. Manero, "On shear-banding and wormlike micellar system response under complex flow," Ann. T. Nord. Soc. Rheol. **25**, 197-203 (2017).

[13]S. Hooshyar and N. Germann, “Shear Banding in 4:1 Planar Contraction,” Polymers **11**,417 1-16 (2019).

[14]S. Varchanis, S.G. Haward, J. Tsamopoulos, and A.Q. Shen, “Evaluation of constitutive models for shear-banding wormlike micellar solutions in simple and complex flows,” J. Non-Newton. Fluid Mech. **307**, 104855 (2022).

[15]E. J. Nodoushan, Y. J. Lee, G. H. Lee, and N. Kim, “Quasi-static secondary flow regions formed by microfluidic contraction flows of wormlike micellar solutions,” Phys. Fluids **33**, 093112 (2021).

[16]P. Fischer and H. Rehage, “Non-linear flow properties of viscoelastic surfactant solutions,” Rheol. Acta **36**, 13–27 (1997).

[17]C. J. Pipe, N. J. Kim, P. A. Vazquez, L. P. Cook, and G. H. McKinley, “Wormlike micellar solutions: II. Comparison between experimental data and scission model predictions,” J. Rheol. **54**, 881–913 (2010).

[18]P. D. Olmsted, O. Radulescu, and C. Y. F. Lu, “Johnson-Segalman model with a diffusion term in a cylindrical Couette flow,” J. Rheol. **44**, 257–275 (2000).

[19]D. Vlassopoulos and S. G. Hatzikiriakos, “A generalized Giesekus constitutive model with retardation time and its association to the spurt effect,” J. Non-Newton. Fluid Mech. **57**, 119–136 (1995).

[20]A. K. Gurnon and N. J. Wagner, “Large amplitude oscillatory shear (LAOS) measurements to obtain constitutive equation model parameters: Giesekus model of banding and nonbanding wormlike micelles,” J. Rheol. **56**, 333–351 (2012).

[21]P. A. Vazquez, G. H. McKinley, and L. P. Cook, “A network scission model for wormlike micellar solutions I. Model formulations and viscometric flow predictions,” J. Non-Newton. Fluid Mech. **144**, 122–139 (2007).

[22]N. Germann, L. P. Cook, and A. N. Beris, “Nonequilibrium thermodynamic modeling of the structure and rheology of concentrated wormlike micellar solutions,” J. Non-Newton. Fluid Mech. **196**, 51–57 (2013).

[23]P. Sollich, “Rheological constitutive equation for a model of soft glassy materials,” Phys. Rev. E **58**, 738-759 (1998).

[24]R. Radhakrishnan and S. M. Fielding, “Shear banding in large amplitude oscillatory shear (LAOStrain and LAOStress) of soft glassy materials,” J. Rheol. **62**, 559 (2018).

[25]G. Ianniruberto and G. Marrucci, “Shear banding in Doi–Edwards fluids,” J. Rheol. **61**, 93–106 (2017).

[26]R. L. Moorcroft and S. M. Fielding, “Shear banding in time-dependent flows of polymers and wormlike micelles,” J. Rheol. **58**, 103–147 (2014).

[27]S. Dutta and M. D. Graham, “Mechanistic constitutive model for wormlike micelle solutions with flow-induced structure formation,” J. Non-Newton. Fluid Mech. **251**, 97–106 (2018).

[28]R. J. Hommel, M. D. Graham, “Constitutive modeling of dilute wormlike micelle solutions: Shear-induced structure and transient dynamics,” J. Non-Newton. Fluid Mech. 295, 104606 (2021).

[29]J. E. López-Aguilar, M. F. Webster, H. R. Tamaddon-Jahromi, and O. Manero, “Predictions for circular contraction-expansion flows with viscoelastoplastic & thixotropic fluids,” J. Non-Newton. Fluid Mech. **261**, 188–210 (2018).

[30]J. E. López-Aguilar, O. Resendiz-Tolentino, H. R. Tamaddon-Jahromi, M. Ellero and O. Manero, “Flow past a sphere: Numerical predictions of thixo-viscoelastoplastic wormlike micellar solutions,” J. Non-Newton. Fluid Mech. **309**, 104902 (2022).

[31]J. P. García-Sandoval, O. Manero, F. Bautista, and J. E. Puig, “Inhomogeneous flows and shear-banding formation in micellar solutions: predictions of the BMP model,” J. Non-Newton. Fluid Mech. **179-180**, 43–54 (2012).

[32]J. E. López-Aguilar, M. F. Webster, H. R. Tamaddon-Jahromi, and O. Manero, “A new constitutive model for worm-like micellar systems - Numerical simulation of confined contraction-expansion flows,” J. Non-Newton. Fluid Mech. **204**, 7–21 (2014).

[33]C. Sasmal. “Flow of wormlike micellar solutions through a long micropore with step expansion and contraction,” Phys. Fluids **32**, 013103 (2020).

[34]J. P. Cunha, P. R. de Souza Mendes, and I. R. Siquera, “Pressure-driven flows of a thixotropic viscoplastic material: Performance of a novel fluidity-based constitutive model,” Phys. Fluids **32**, 123104 (2020).

[35]D. Broboana, C. S. Ionescu, and C. Balan, "Numerical modelling of the shear banding flow in the proximity of micro-structures," 10th International Symposium on Advanced Topics in Electrical Engineering (ATEE), Bucharest, Romania, 483-486 (2017), DOI: 10.1109/ATEE.2017.7905156.

[36]Z. Tadmor and C. G. Gogos, *Principles of Polymer Processing* (Wiley-Interscience, 2006).

[37]J. E. López-Aguilar, M. F. Webster, H. R. Tamaddon-Jahromi, and O. Manero, “High-Weissenberg predictions for micellar fluids in contraction-expansion flows,” J. Non-Newton. Fluid Mech. **222**, 190–208 (2015).

[38]J. E. López-Aguilar, M. F. Webster, H. R. Tamaddon-Jahromi, and O. Manero, “Convoluted models and high-Weissenberg predictions for micellar thixotropic fluids in contraction–expansion flows,” J. Non-Newton. Fluid Mech. **232**, 55–66 (2016).

[39]K. A. Carter, J. M. Girkin, and S. M. Fielding, “Shear banding in large amplitude oscillatory shear (LAOStrain and LAOStress) of polymers and wormlike micelles,” J. Rheol. **60**, 883–904 (2016).

[40]M. M. Britton, R. W. Mair, R. K. Lambert, and P. T. Callaghan, “Transition to shear banding in pipe and Couette flow of wormlike micellar solutions,” J. Rheol. **43**, 897–909 (1999).

Table and figure captions

Table 1. Deformation-rate versus fluid chart

Table 2. List of parameters

Figure 1. Schematics of the planar *modified* Couette geometry – This complex flow geometry is a composition of a 4:1:4 planar contraction-expansion with rounded edges and a drag flow. The flow is promoted by the drag the sliding plate exerts on the fluid stick to its surface. One observes simple-shear flow away from the contraction and mixed shear-to-extensional flow in the contraction neighbourhood.

Figure 2. a) T_{xy} , b) *viscosity*, and c) N_{1Shear} against deformation-rate (simple shear & uniaxial extension); β=10^{-2}; BMP+_τ_p: {ω, ξ_{G0}, ξ, δ}={4, 0.1136, 2.27x10^{-7}, 1x10^{-6}}, non-shear-banding fluid (ζ=0), shear-banding fluid (ζ=3); VCM: {C_{Aeq}, C_{Beq}, ξ, ε, μ}={0.5, 0.7, 0.42, 7.5x10^{-7}, 1.5}.

Figure 3. a) T_{xy}, b) N_{1Shear} and c) f against shear-rate (simple shear flow); BMP+_τ_p; {ω, ξ_{G0}, ξ, δ}={4, 0.1136, 2.27x10^{-7}, 1x10^{-6}}; shear-banding fluid (ζ=3)

Figure 4. a) Normal-stress T_{xx} and b) shear-stress T_{xy} profiles sampled at the upstream fully-developed region; β=10^{-2}, {ω, ξ_{G0}, ξ, δ}={4, 0.1136, 2.27x10^{-7}, 1x10^{-6}}; mesh-refinement study for coarse, medium and refined grids; Case E: shear-banding fluid (ζ=3)

Figure 5. a) Velocity U_x , b) shear-rate $\partial U_x/\partial$y, c) viscosity, d) f-functional, e) shear-stress T_{xy}, f) normal-stress T_{xx} and g) pressure P fields; β=10^{-2}, {ω, ξ_{G0}, ξ, δ}={4, 0.1136, 2.27x10^{-7}, 1x10^{-6}}; Case E: shear-banding fluid (ζ=3)

Figure 6. Profiles of a) U_x b) U_y , c) T_{xy} and d) U_x @ contraction-gap; β=10^{-2}, {ω, ξ_{G0}, ξ, δ}={4, 0.1136, 2.27x10^{-7}, 1x10^{-6}}; Case E: shear-banding fluid (ζ=3)

Figure 7. a) T_{rz} , b) η_{Shear} and η_{Ext}, and c) N_{1Shear} against deformation-rate (simple shear & uniaxial extension); BMP+_τ_p; β=10^{-2}, {ω, ξ_{G0}, ξ, δ}={4, 0.1136, 2.27x10^{-7}, 1x10^{-6}}; Case E: shear-banding fluid (ζ=3)

Figure 8. Banded-solution profiles: entry-analytic vs exit-Non-SCP; a) velocity U_x , b) shear-rate $\partial U_x/\partial$y, c) normal-stress T_{xx}, d) shear-stress T_{xy}, e) f-functional, f) viscosity; BMP+_τ_p; β=0.01, {ω, ξ_{G0}, ξ, δ}={4, 0.1136, 2.27x10^{-7}, 1x10^{-6}}; Case E: shear-banding fluid (ζ=3)

Figure 9. Banded-solution profiles under shock captures: analytic-entry vs exit-SCP; SCP-f: a) shear-stress T_{xy}, b) normal-stress T_{xx}; SCP-Vgrad: c) T_{xy}, d) T_{xx}; SCP-f-Vgrad: e) T_{xy}, f) T_{xx}; BMP+_τ_p; β=0.01, {ω, ξ_{G0}, ξ, δ}={4, 0.1136, 2.27x10^{-7}, 1x10^{-6}}; Case E: shear-banding fluid (ζ=3)

Figure 10. a) Velocity U_x , b) shear-rate $\partial U_x/\partial$y, c) viscosity, d) *f*-functional, e) shear-stress T_{xy}, f) normal-stress T_{xx} and g) pressure *P* fields; β=10^{-2}, {ω, ξ_{G0}, ξ, δ}={4, 0.1136, 2.27x10^{-7}, 1x10^{-6}}; Case B: non-shear-banding fluid (ζ=0)

Figure 11. a) Velocity U_x , b) shear-rate $\partial U_x/\partial$y, c) viscosity, d) *f*-functional, e) shear-stress T_{xy}, f) normal-stress T_{xx} and g) pressure *P* fields; β=10^{-2}, {ω, ξ_{G0}, ξ, δ}={4, 0.1136, 2.27x10^{-7}, 1x10^{-6}}; Case D: shear-banding fluid (ζ=3)

Figure 12. a) Velocity U_x , b) shear-rate $\partial U_x/\partial$y, c) viscosity, d) *f*-functional, e) shear-stress T_{xy}, f) normal-stress T_{xx} and g) pressure *P* fields; β=10^{-2}, {ω, ξ_{G0}, ξ, δ}={4, 0.1136, 2.27x10^{-7}, 1x10^{-6}}; Case A: non-shear-banding fluid (ζ=0)

Figure 13. a) Velocity U_x , b) shear-rate $\partial U_x/\partial$y, c) viscosity, d) *f*-functional, e) shear-stress T_{xy}, f) normal-stress T_{xx} and g) *P* fields;β=10^{-2}, {ω, ξ_{G0}, ξ, δ}={4, 0.1136, 2.27x10^{-7}, 1x10^{-6}}; Case C: non-shear-banding fluid (ζ=0)